# Stability Analysis for the Grid-Connected Single-Phase Asymmetrical Cascaded Multilevel Inverter with SRF-PI Current Control under Weak Grid Conditions

Han, Yang; Chen, Hao; Li, Zipeng; Yang, Ping; Xu, Lin; Guerrero, Josep M.

*Published in:*
IEEE Transactions on Power Electronics

*DOI (link to publication from Publisher):*
10.1109/TPEL.2018.2867610

*Publication date:*
2019

*Document Version*
Accepted author manuscript, peer reviewed version

This article has been accepted for publication in a future issue of this journal, but has not been fully edited. Content may change prior to final publication. Citation information: DOI 10.1109/TPEL.2018.2867610, IEEE Transactions on Power Electronics

# Stability Analysis for the Grid-Connected Single-Phase Asymmetrical Cascaded Multilevel Inverter with SRF-PI Current Control under Weak Grid Conditions

Yang Han, *Senior Member*, *IEEE*, Hao Chen, Zipeng Li, Ping Yang, Lin Xu and Josep M. Guerrero, *Fellow*, *IEEE*

***Abstract*-This paper analyzes the influence of phase-locked loop (PLL) on the stability of LCL-type single-phase grid-connected asymmetrical cascaded H-bridge multilevel inverter (ACHMI) with synchronous reference frame proportional-integral (SRF-PI) grid current control under weak grid scenarios. The ACHMI system is composed of power stage circuit and control system, where the control system contains the dual-loop current control strategy established in the hybrid reference frame (HRF), the synchronous reference frame PLL (SRF-PLL) and the hybrid modulation method employed to synthesize the multilevel output voltage. The small-signal model of the whole ACHMI system is first established by using a simple step-by-step derivation method, and then, the small-signal analysis method is adopted to linearize the ACHMI, which is then utilized to derive the impedance model of the ACHMI system. Furthermore, an improved impedance stability criterion is derived, which is then employed to analyze the system stability. By using this criterion, the stability of the ACHMI can be evaluated with the variation of the bandwidth of PLL, the output power factor angle of the ACHMI and the amplitude of the grid current reference signal under weak grid conditions. In this paper, a systematic design procedure for the optimal selection of the proportional-integral (PI) controller of the PLL is presented, which guarantees the steady-state performance and dynamic response of the ACHMI system. With this design method, the dual-loop current control and PLL can be taken into account simultaneously when analyzing the stability margin of the ACHMI. Finally, the simulation and experimental results from a down-scaled grid-connected ACHMI prototype system are provided to confirm the validity of theoretical analysis.**

***Index Terms*—Phase-locked loop (PLL), asymmetrical cascaded H-bridge multilevel inverter (ACHMI), small-signal model, impedance stability criterion, weak grid**

## I. Introduction

The single-phase grid-connected cascaded H-bridge multilevel inverters (CHMI) are increasingly employed in various industrial fields, and play a critical role in converting the power produced by distributed power generation systems (DPGS) into high quality ac power and injecting into the grid reliably [1], [2], [3]-[9]. Compared to the single-phase H-bridge inverters [10], diode-clamped inverters [11] and capacitor-clamped inverters [12], the CHMIs have attracted more attention due to its advantages of easy modularization and flexible extension to higher voltage levels. In retrospect, CHMI contains the symmetrical topologies [4], [5] and asymmetrical topologies [6-9]. In general, each H-bridge in symmetrical topology has same value of the input DC voltage. Whereas, each H-bridge in asymmetrical topology has different value of the input DC voltage, usually scaled in {1:2:4…}, {1:3:9…} or {1:2:6…}. Compared to the symmetrical topology, the asymmetrical topology has attracted more interest due to its advantage of the capability to maximize the numbers of output voltage levels. Currently, most of literatures focus on the modulation strategies and control methods of the asymmetrical cascaded H-bridge multilevel inverter (ACHMI) and little work has been done on the stability analysis based on the single-phase grid-connected ACHMI system [8], [9], [13-15].

Generally, current control and phase-locked loop (PLL) are essential for the grid-connected inverter system, and both of them have effects on the stability of the grid-connected inverter [16-22]. The stability problems caused by current control have been widely discussed in recent literatures [16-20], [33], [34]. Besides, the impact of the PLL on the system stability can be introduced by the grid reference current, and its phase is derived from the detection of the voltage at the point of common coupling (PCC) by a PLL [21], [22]. Therefore, the effects of PLL on the stability of the grid-connected inverter cannot be neglected in stability analysis. However, most of the existing literature only consider the influence of the current control or the effect of PLL when analyzing the stability of the grid-connected inverters [16]-[26].

In [16]-[20], a variety of works have been done to enhance the stability and dynamic performance of the grid-connected inverters by improving the current control method and optimized design of the system parameters. For instance, a design recommendation of LCL-filter parameters and control gain based on the Jury stability criterion is given to increase the robustness of a grid-connected inverter with LCL-filter in [17]. In [18], a pseudo-derivative-feedback (PDF) control method based on the current feedback is suggested to enhance the dynamic response of the three-phase grid-connected inverter. To improve the system stability under grid voltage disturbance conditions, a direct grid current control method has been proposed and the proportional resonant (PR) plus harmonic compensator (PR+HC) structure is adopted [19]. In [20], a single-loop current control with a hybrid damper is proposed for grid-tied inverter based on the high-order power filter to overcome the impact of the background harmonic voltage and the wide variation of equivalent grid impedance. Although the system stability and dynamic performance can be improved by using the methods proposed in [16]-[20], the effects of PLL on the stability of the grid-connected inverter is neglected.

Manuscript received January 14, 2018; revised April 1, 2018 and July 31, 2018; accepted August 25, 2018. Date of publication *******; date of current version *******. This work was supported in part by the National Natural Science Foundation of China (NSFC) under grant No. 51307015, and in part by Sichuan Province Key Research and Development Project under grant No.2017GZ0347, and in part by Natural Science Foundation of Guangdong Province under grant No.2018A030313494. Recommended for publication by Associate Editor *****.

Y. Han, H. Chen and P. Yang are with the School of Mechanical and Electrical Engineering, University of Electronic Science and Technology of China, No.2006, Xiyuan Avenue, West Hi-Tech Zone, Chengdu 611731, China (e-mail: hanyang@uestc.edu.cn; 695416077@qq.com; ping@uestc.edu.cn).

Z. Li is with State Grid Guanghan City Electric Power Supply Branch, Guanghan 618300, China (zroc.lee@qq.com)

L. Xu is with the Sichuan Electric Power Research Institute, No.16 West Jinhui Road #2, Chengdu 610072, China (xulinn@163.com).

J. M. Guerrero is with Department of Energy Technology, Aalborg University, 9220 Aalborg, Denmark (e-mail: joz@et.aau.dk).

Color versions of one or more of the figures in this paper are available online at http://ieeexplore.ieee.org.

Digital Object Identifier ******/TPEL.*******

This article has been accepted for publication in a future issue of this journal, but has not been fully edited. Content may change prior to final publication. Citation information: DOI 10.1109/TPEL.2018.2867610, IEEE Transactions on Power Electronics

In [21]-[26], some works have been done on enhancing the stability and dynamic performance of the grid-connected inverter by improving the performance of PLL. In [23], a new control algorithm based on PLL is developed to improve the performance of PLL. As a consequence, the system stability can be improved under three-phase grid voltage harmonics and unbalance scenarios. Considering the effects of the phase offset error and double-frequency on system stability, the transfer delay-based PLL (TD-PLL) is modified as an adaptive transfer delay-based PLL [24]. In [25]-[26], it can be found that the selection of PLL bandwidth has remarkable impacts on the system stability for the grid-connected inverter under weak grid conditions. Clearly, the stability of the grid-connected inverter can be enhanced by improving the performance of PLL. Without doubt, only the influence of PLL is mentioned when analyzing the system stability in [21]-[26] and the impact of current control on the grid-connected system stability is overlooked. Thus, it is necessary to consider current control and PLL simultaneously when analyzing the stability of the grid-connected inverter system.

There are few papers simultaneously consider the effects of PLL and current control on system stability for the grid connected inverters [27-30]. In [27], the negative effect of PLL on current control under weak grid condition is investigated, and then, an improved design of current controller parameters and capacitor current feedback method is proposed. Although the ability of current control to reduce the negative influence of PLL is improved with the proposed method, it results in high complexity and is mainly designed for three-phase grid-connected inverters. In [28], an unified impedance model is proposed to analyze the dynamic response of the grid-connected inverter caused by the PLL and current control, and the generalized Nyquist stability criterion (GNSC) is used for the converter-grid interaction analysis. However, only the effect of the control bandwidth of the synchronous reference frame PLL (SRF-PLL) on the system stability is discussed, and the studied system was still a three-phase system. The stability of the single-phase grid-connected inverter system is studied in [29], where the dynamic phasor approach is adopted to determine the 2-D source and load impedances, and the GNSC is employed to evaluate system stability. However, the influences of the parameters on system stability and the design of the PLL parameters have not been reported. In [30], the effect of current control and PLL are considered when analyzing the stability of the three-phase system, and the controller parameters of PLL is also discussed. However, the parameter design of PLL, the effects of the amplitude of reference current and power angle on system stability are not discussed.

Thus, this paper aims to analyze the influences of PLL, the amplitude of reference current and power factor angle on the LCL-type single-phase grid-connected ACHMI system and provide parameter design guideline for PLL under this scenario. In consideration of the integrity of the stability analysis in this work, the double-loop current control method built in hybrid reference frame and the hybrid modulation strategy are simultaneously considered.

In view of the system modelling, it is well-known that the Linear Periodic (LTP) theory can be used for the single-phase system modelling. The LTP model can be obtained by using the harmonic linearization on the average model of the studied single-phase system [31]. And the application of the LTP theory is based on the linearization of the full-order differential equation model of the system. However, the single-phase asymmetric cascaded H-bridge inverter is more complex than the conventional single-phase H-bridge inverter. If the linearization for the full-order differential equation model of the studied system is established, the complexity of calculation and analysis would be significantly increased. Obviously, the technique that the linearization for the full-order differential equation model of the system is not suitable for the impedance analysis method, which is adopted for the stability analysis in this paper.

Besides, a dual-loop current control strategy, composed by an inner current loop based on feeding back the LCL-filter capacitor current and an outer grid current loop, is presented in the studied system. Without doubt, the selection of the grid current controller is crucial for high quality current control of the grid-connected inverter [19]. It is well known that the proportional-resonant (PR) controller is a popular choice for the single-phase AC system due to the ability to eliminate the tracking error [32]. However, the PR controller exhibits a poor dynamic performance under input signal variation scenarios [33]. To overcome this drawback, the synchronous reference frame proportional-integral (SRF-PI) controller is adopted to control the grid current [34]-[35], which achieves the zero steady-state error, and guarantees a good dynamic performance.

The SRF-PI control scheme is a well-developed technique in three-phase PWM converters, which contains two conventional PI controller with the identical parameters, can also be extended to single-phase systems [34]-[35]. In addition, the inner current loop is controlled by proportional controller in the stationary frame, which is the simplest way to regulate the current and enhance the dynamic performance of the system at the same time. In the proposed approach, the control of the inner current loop is realized in stationary frame and the control of the outer current loop is achieved in dq frame. Therefore, the dual-loop current control strategy is conducted in the hybrid reference frame in this paper. And then, the system model is also established in the hybrid reference frame, which is different from the modelling method in the dq frame. For the generality of the stability analysis, a conventional SRF-PLL is adopted for grid synchronization. Finally, the validity of the modelling method is verified by the theoretical analysis, the simulation and experimental results. The main contributions of this paper are summarized as follows:

1) The double-loop current control method established in hybrid frame is proposed in this paper to control the LCL-type grid-connected single-phase ACHMI, where the control of the outer current loop is built in *dq* frame and inner control loop is realized in the stationary reference frame. The small-signal model of the single-phase ACHMI with this control strategy is developed based on a simple step-by-step calculation method.

2) The hybrid modulation method is employed to modulate the single-phase ACHMI system. The detailed analysis of the hybrid modulation with small disturbance is presented. With this analysis, under the small disturbance condition, the small-signal model of the hybrid modulation process has been derived, and it is found that the hybrid modulation can be approximated to a proportional gain with a control delay.

3) A systematic impedance model of the grid-connected ACHMI is established, which contains both dual-loop current control loop, hybrid modulation and PLL loop. With this model, the effect of PLL, grid current reference amplitude $I_{Am}$ and power factor angle $\varphi$ on the system stability can be easily analyzed, and it is convenient to design controller parameters of PLL, which contributes to enhance the system stability and dynamic performance under weak grid conditions. Finally, the control method and the parameter design guidelines are substantially confirmed by the simulation and experimental results.

This paper is organized as follows. In Section II, the system structure of the LCL-type grid-connected single-phase ACHMI is presented. The dual-loop current control strategy based on hybrid reference frame and the hybrid modulation method are also analyzed. In Section III, a systematic small-signal model of the single-phase ACHMI system with PLL is proposed. In Section IV, the stability of the grid-connected ACHMI is studied under weak grid conditions and a systematic controller parameter

This article has been accepted for publication in a future issue of this journal, but has not been fully edited. Content may change prior to final publication. Citation information: DOI 10.1109/TPEL.2018.2867610, IEEE Transactions on Power Electronics

design method for the PLL is presented. Section V and Section VI presents simulation the results and experimental results, respectively. Finally, Section VII concludes this paper.

## II. LCL-Type Grid-Connected Asymmetrical Cascaded H-Bridge Multilevel Inverter

Fig. 1 illustrates the single-phase LCL interfaced grid-connected ACHMI, which contains the power stage and control system. As shown in Fig. 1, the power stage of the ACHMI is composed of three standard H-bridge Cells denoted as Cell1 (low voltage Cell), Cell2 (medium voltage Cell), and Cell3 (high voltage Cell) respectively, and connected to the grid through LCL filter, which consists of the inverter-side inductance $L_1$, filter capacitor $C$, and the grid-side inductance $L_2$. Grid voltage and the equivalent grid impedance are represented by $v_g$ and $Z_g$, respectively.

In the power stage of the ACHMI, $v_i$ represents the output voltage of the ACHMI, $i_1$ denotes the inverter-side current, $v_c$ denotes the capacitor voltage. The sampling switch of the capacitor current $i_c$ and grid current $i_g$ is represented by $SW_1$ and $SW_2$, respectively. The $u_{PCC}$ denotes the voltage at the point of common coupling (PCC), where $u_{PCC}$ is sampled for the phase-locked-loop (PLL). Besides, each H-bridge Cell is provided with a constant and isolated DC source, where the ratio of DC voltage is 1:2:6 and the DC voltage of Cell1 is the lowest among the three Cells. By applying the hybrid modulation method into ACHMI, each H-bridge Cell can generate a three-level output voltage with different switching frequencies.

The control system of the ACHMI contains the current control and hybrid modulation. The dual-loop current control method established in hybrid reference frame is shown in Fig. 1, where the SRF-PI controller established in $dq$ reference frame is adopted in the outer grid current loop and the proportional controller $K$ established in stationary reference frame is used in the inner current loop [34]-[35]. Specifically, to emulate a two-phase systems, $i_g$ and grid reference current $i_{g,ref}$ are taken as the $\alpha$-axis input $i_\alpha$ and $i_{\alpha,ref}$ for the Park's transformation, respectively, and two fictitious electrical signals, generated by the time delay block, are used as the $\beta$-axis input $i_\beta$ and $i_{\beta,ref}$ [35]. In order to ensure a zero steady-state error, two identical conventional PI controllers in the SRF are employed to regulate the current signals in $d$-axis and $q$-axis. And then, the output of the PI controllers are transformed back to the stationary frame by using the inverse Park's transformation, and the $\alpha$-axis output current $i^*_{C,\alpha}$ is taken as the reference for $i_c$. The inner current $i_c$ loop with a proportional controller $K$ is mainly used to provide active damping and improve the system dynamic performances [35]. Subsequently, the signal $U_m$ obtained from the output of inner current loop is used as modulation signal for the modulation process. Due to the difference of the studied inverter topology and the common single-phase two-level grid-connected inverter topology, the hybrid modulation method is adopted. In order to systematically study the stability of the LCL-type single-phase grid-connected asymmetric cascaded H-bridge multilevel inverter, the hybrid modulation method is analyzed as follows.

Fig. 2 illustrates the structure of the hybrid modulation strategy, which is specially designed for the ACHMI and contributes to

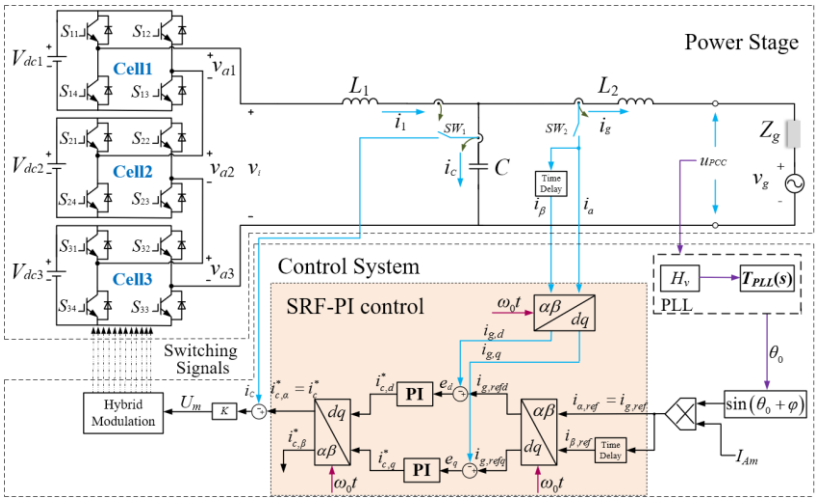


Fig.1. Block diagram of the single-phase LCL interfaced grid-connected ACHMI system.

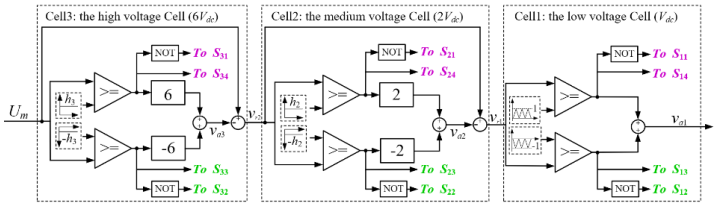


Fig. 2. Block diagram of the hybrid modulation process of the grid-connected ACHMI system.

achieving the maximized output voltage level of ACHMI [36], where the input DC voltage $V_{dc1}$, $V_{dc2}$ and $V_{dc3}$ of the ACHMI is set as $V_{dc}$, $2V_{dc}$ and $6V_{dc}$, respectively. The detailed operation principle of hybrid modulation method is shown in Fig. 3. From Fig. 3, it can be observed that Cell3 commutates when $U_m$ reaches $\pm h_3$ to generate a three-level voltage waveform. After determining the output voltage $v_{a3}$ of the Cell3, the reference signal $v_{r2}$ of Cell2 can be obtained by subtracting the output voltage $v_{a3}$ of Cell3 from $U_m$. And then, $v_{r2}$ is compared to $\pm h_2$ to generate Cell2 waveform $v_{a2}$. Finally, the reference signal $v_{r1}$ of Cell1 is compared with two high frequency triangular carriers, resulting in a high-frequency output voltage $v_{a1}$. The output signal

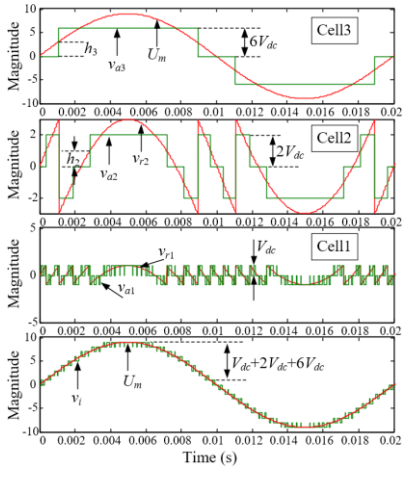


Fig. 3. The generation of output voltage waveforms in ACHMI with DC voltage ratio of 1:2:6 [36].

This article has been accepted for publication in a future issue of this journal, but has not been fully edited. Content may change prior to final publication. Citation information: DOI 10.1109/TPEL.2018.2867610, IEEE Transactions on Power Electronics

$v_i$ is synthesized by $v_{a1}$, $v_{a2}$ and $v_{a3}$, as shown in Fig. 3. It should be emphasized that the comparative level ($h_3$, $h_2$) has been selected in a way that the unmodulated part can be produced by Cell1 to avoid over-modulation. If we consider that the maximum amplitude that can be produced by the ACHMI is $V_{dc}$+2$V_{dc}$+6$V_{dc}$, the only way to avoid over-modulation is that the unmodulated part does not exceed the total voltage left for Cell1. Thus, $h_3$=2$V_{dc}$+$V_{dc}$ for Cell3 and $h_2$=$V_{dc}$ for Cell2. Finally, the last unmodulated part is generated by Cell1.

According to Fig. 2, the Sine Pulse Width Modulation (SPWM) is adopted for the Cell1. By using the state averaging technique in one PWM cycle of the Cell1, the SPWM process can be approximated by a proportional control loop. And the proportional coefficient is the DC voltage $V_{dc}$ of the Cell1. After analyzing the hybrid modulation, the whole output voltage of the hybrid modulation is $U_m V_{dc}$ with different initial input of the modulation signal $U_m$ in one PWM cycle of the Cell1. Besides, the sampling period $T_s$ is the same as the PWM cycle in the digital control of Cell1. The hybrid modulation is completed in one fundamental cycle. Considering the sampling and calculation delay of one PWM cycle, and the delay of zero-order holder (ZOH) of half a PWM cycle, the hybrid modulation has effect on stability of the system due to the delay.

The diagram of the hybrid modulation with small disturbance is shown in Fig. 4, where Fig. 4(a), Fig. 4(b) and Fig. 4(c) denotes the modulation of Cell3, Cell2 and Cell1, respectively. In Fig. 4(a), $U_m$ represents the steady-state modulation signal and the modulation signal with disturbance of Cell3 is denoted as $u_m$. The carrier signals represented by $v_{c3}$ are constant DC signals. $s_{3,1}$ and $s_{3,2}$ characterize the output waveforms under disturbance condition, and the output waveforms under steady-state condition are represented by $S_{3,1}$ and $S_{3,2}$. It can be seen that Cell3 has two switching states, i.e., $S_{3,1}$ ($s_{3,1}$) and $S_{3,2}$ ($s_{3,2}$). The switching devices $S_{31}$ and $S_{33}$ are conducting under state $S_{3,1}$ ($s_{3,1}$), where a rectangular waveform with an amplitude of 6$V_{dc}$ can be obtained. The switching devices $S_{32}$ and $S_{34}$ are conducting under state $S_{3,2}$ ($s_{3,2}$), where a rectangular waveform with an amplitude of -6$V_{dc}$ can be obtained.

When there is some disturbance in the modulation signal, whose amplitude is much smaller than that of the steady-state modulation signal $U_m$, the obtained rectangular waveform of $v_{a3}$ would contain disturbance component, which can be represented by $\hat{s}_3$. Due to the small amplitude of the disturbance existed in the modulated signal and the adopted DC carrier signal, the disturbance $\hat{s}_3$ of the output voltage can be considered as voltage pulse with extremely narrow width. Besides, $\hat{s}_3$ only appears on the rising and falling edges of the rectangular waveform produced under the steady-state condition, and so there are four $\hat{s}_3$ in each fundamental period. However, the widths of these four voltage pulses are much smaller than the width of the rectangular waveforms produced under the steady-state condition in one fundamental period.

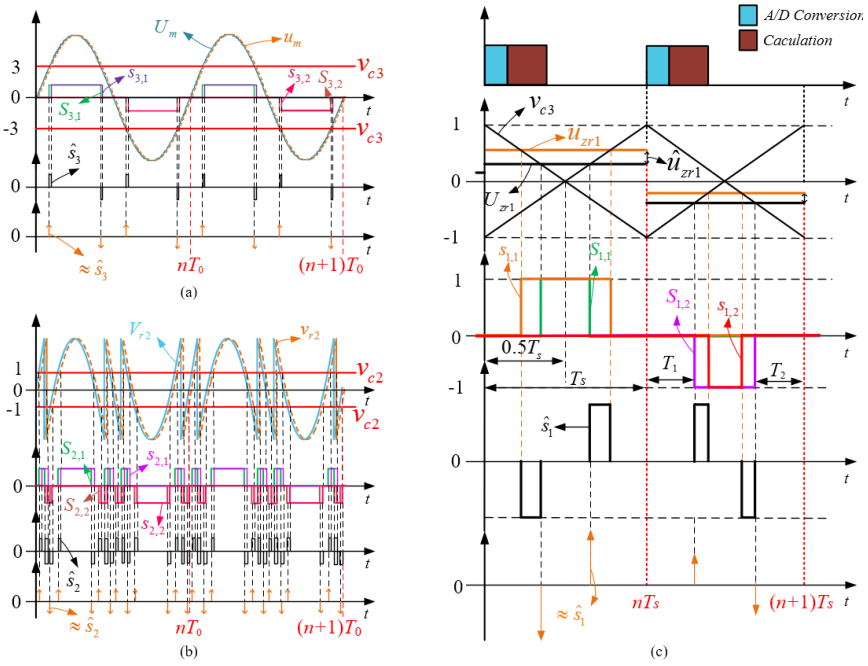


Fig. 4 Diagram of the hybrid modulation with small disturbance: (a) the high voltage Cell (Cell3) (b) the medium voltage Cell (Cell2) (c) the low voltage Cell (Cell1)

Hence, the influence caused by these four voltage pulses can be neglected. Namely, the effect came from the disturbance in the modulation signal on high voltage Cell can also be omitted. It can be seen that the carrier signals are also DC signals in medium voltage Cell shown in Fig. 4(b). Similarly, the same analysis method is employed to Cell2, and then, a conclusion can be obtained that the influence came from the disturbance in the modulation signal on Cell2 can also be ignored. Therefore, the effect of the disturbance in the modulation signal only appears on Cell1, where the SPWM method is adopted.

As shown in Fig. 4(c), $U_{zr1}$ represents the steady-state modulation signal of the Cell1, and the modulation signal with disturbance of the Cell1 is represented by $u_{zr1}$. The disturbance of the modulation signal is denoted as $\hat{u}_{zr1}$. $s_{1,1}$ and $s_{1,2}$ characterize the output waveforms under disturbance condition, and the steady-state output signals are represented by $S_{1,1}$ and $S_{1,2}$. The output voltage $\hat{s}_1$, caused by $\hat{u}_{zr1}$, can be obtained by subtracting the output voltage under disturbance condition from the output voltage under steady-state condition, where the signal $\hat{s}_1$ is also considered as impulse signal.

If the initial time of the each switching period is considered as $t$=0, the expression of $\hat{s}_1$ in time domain can be written as (1) through equivalent calculation:

$$\hat{s}_1(t) \approx \frac{1}{2} T_s \left[ \delta(t - T_1) + \delta\left(t - (T_s - T_2)\right) \right] \tag{1}$$

where $T_1$ and $T_2$ are shown in Fig. 4(c). By applying the Laplace transform to both sides of (1), we get:

$$\hat{s}_1(s) = \frac{T_s}{2} \left( e^{-sT_1} + e^{-s(T_s - T_2)} \right) \tag{2}$$

According to digital control theory, there is a switching period between the sampling time and the updated time of duty cycle. Hence, Eq. (2) should be rewritten as (3), which is the transfer function of the hybrid modulation under disturbance.

This article has been accepted for publication in a future issue of this journal, but has not been fully edited. Content may change prior to final publication. Citation information: DOI 10.1109/TPEL.2018.2867610, IEEE Transactions on Power Electronics

$$\hat{s} \approx \hat{s}_1(s) \approx \frac{e^{-1.5sT_s}}{2} T_s \underbrace{\left( e^{-\frac{D}{2}sT_s} + e^{\frac{D}{2}sT_s} \right)}_{\Delta e} \tag{3}$$

where $D$ represents the duration of the state $S_{1,1}$ or $S_{1,2}$, and can be equivalent to the duty cycle. From Eq. (3), it can be seen that the hybrid modulation under small disturbance is approximated to a delay link, whereas the values of Eq. 3 have very little difference when $D$ is changing within (0,1) [37].

Moreover, it is assumed that $\Delta e = e^{-0.5DsT_s} + e^{0.5DsT_s}$ to simplify calculation, and Taylor series expansion method is adopted to simplify $\Delta e$. Since the value of $T_s$ is extremely small, so the high order items of $T_s$ can be ignored. As a result, $\Delta e$ can be approximated to 2, and Eq. (3) is then simplified as:

$$G_{d1}(s) \approx T_s e^{-1.5sT_s} \tag{4}$$

In discrete domain, the frequency responses of the two sampling switches of the grid current $i_g$ and capacitor current $i_c$ can be considered as $1/T_s$, as discussed in [38]. Therefore, the $1/T_s$ is also considered in the whole modulation in continuous model. As a consequence, the modulation delay of the Cell1 can be written as:

$$G_{hy}(s) = G_{d1}(s) \cdot \frac{1}{T_s} \approx e^{-1.5sT_s} \tag{5}$$

Therefore, the hybrid modulation under small disturbance condition can be approximated as $e^{-1.5sT_s}$ by combining the analysis about the modulation process based on the three individual Cells.

## III. Small-Signal Modeling

The impedance-based stability analysis is employed to investigate the impact of PLL on the LCL-type grid-connected ACHMI under weak grid condition. Hence, in order to obtain the impedance model of the whole system, the small-signal models of the ACHMI and PLL are derived in this section.

### *A. Small-Signal Model of the ACHMI*

Referring to Fig. 1, the small-signal models of the ACHMI include two parts, i.e., the power stage and the control system, which are modeled simultaneously in the following parts by using a simple step-by-step model derivation approach.

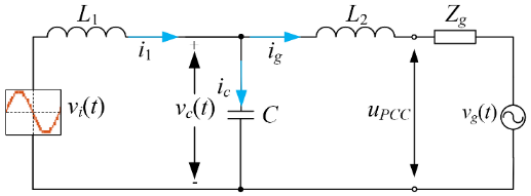


Fig. 5 The simplified power-stage circuit of the ACHMI.

**Step 1:** Derive the small-signal model of the power stage circuit. According to Fig. 1, the simplified power stage circuit of the ACHMI can be depicted as shown in Fig. 5.

$$\begin{cases} \dfrac{di_1}{dt} = \dfrac{1}{L_1} v_i - \dfrac{1}{L_1} v_c \\ \dfrac{di_g}{dt} = \dfrac{1}{L_2} v_c - \dfrac{1}{L_2} u_{PCC} \\ \dfrac{dv_c}{dt} = \dfrac{1}{C} i_c \\ i_c = i_1 - i_g \end{cases} \tag{6}$$

By applying voltage and current Kichhoff's Laws in the simplified circuit, the model of the power stage can be derived as (6). And then, by using the perturbation and linearization technique [39], the state variables $i_c$, $i_g$, $v_c$, and the input signal $u_{PCC}$ can be replaced by a constant value with a small-signal variation component, as shown in (7).

$$\begin{cases} i_c = I_c + \hat{i}_c \\ i_g = I_g + \hat{i}_g \\ v_c = V_c + \hat{v}_c \\ u_{PCC} = U_{PCC} + \hat{u}_{PCC} \end{cases} \tag{7}$$

Substituting (7) into (6), the small-signal model of the ACHMI power-stage can be derived as:

$$\begin{cases} \dfrac{d\hat{i}_g}{dt} = \dfrac{1}{L_2} \hat{v}_c - \dfrac{1}{L_2} \hat{u}_{PCC} \\ \dfrac{d\hat{i}_c}{dt} = \dfrac{1}{L_1} \hat{v}_i + \dfrac{1}{L_2} \hat{u}_{PCC} - \dfrac{L_1 + L_2}{L_1 L_2} \hat{v}_c \\ \dfrac{d\hat{v}_c}{dt} = \dfrac{1}{C} \hat{i}_c \end{cases} \tag{8}$$

**Step 2:** Calculate the differential equation of the grid current $i_g$. As shown in Fig. 1, it can be clearly seen that $i_g$ is set as $i_\alpha$. And $i_\beta$ can be obtained by applying a delay link $e^{-\tau s}$ to $i_\alpha$, where the delayed length of time $\tau$ is a quarter of grid period [35], that is 0.005s. By using the first-order Pade approximation [40], $e^{-\tau s}$ can be changed as:

$$\frac{i_\beta(s)}{i_\alpha(s)} = e^{-\tau s} \approx \frac{2 - \tau s}{2 + \tau s} \tag{9}$$

According to (9), a differential equation, including $i_\alpha$ and $i_\beta$, can be expressed as (10). And then, Eq. (11) can be obtained when it is assumed that $x_1 = i_\alpha + i_\beta$, where $x_1$ is considered as a new state variable.

$$\tau \left[ \frac{di_\alpha}{dt} + \frac{di_\beta}{dt} \right] = 4i_\alpha - 2\left( i_\alpha + i_\beta \right) \tag{10}$$

$$\frac{dx_1}{dt} = \frac{4}{\tau} i_\alpha - \frac{2}{\tau} x_1 \tag{11}$$

By applying the perturbation and linearization technique [39], the small-signal model of (11) can be written as:

$$\frac{d\hat{x}_1}{dt} = \frac{4}{\tau} \hat{i}_g - \frac{2}{\tau} \hat{x}_1 \tag{12}$$

The differential equation of the reference current $i_{g,ref}$ can also be calculated. From Fig. 1, it can be found that $i_{g,ref}$ has the same transformation process with $i_g$. Therefore, it can be assumed that $x_2$ is a state variable and $x_2 = i_{\alpha,ref} + i_{\beta,ref}$ based on $i_{g,ref}$ ($i_{\alpha,ref}$). As a result, the perturbation equation related to $i_{g,ref}$ can be derived as:

$$\frac{d\hat{x}_2}{dt} = \frac{4}{\tau} \hat{i}_{\alpha,ref} - \frac{2}{\tau} \hat{x}_2 \tag{13}$$

**Step 3:** Derive the reference signal $i_c^*$ of the capacitor current $i_c$. As shown in Fig. 1, through the Park's transformation for $i_\alpha$ and $i_\beta$, the electrical signals $i_{g,d}$ and $i_{g,q}$ can be obtained. Identically, the electrical signals $i_{g,refd}$ and $i_{g,refq}$ can also be obtained after the Park's transformation for $i_{\alpha,ref}$ and $i_{\beta,ref}$. It is assumed that the error signal of the $d$-axis and $q$-axis is represented by $e_d$ and $e_q$, respectively. Hence, $e_d$ is equal to $i_{g,refd} - i_{g,d}$ and $e_q$ is equal to $i_{g,refq} - i_{g,q}$. Substituting (12) and (13) into $e_d$ and $e_q$, the following equation can be derived:

$$\begin{cases} e_d = (\cos\omega_0 t)\left( i_{\alpha,ref} - i_\alpha \right) + (\sin\omega_0 t)\left( x_2 - i_{\alpha,ref} - x_1 + i_\alpha \right) \\ e_q = (\sin\omega_0 t)\left( i_\alpha - i_{\alpha,ref} \right) + (\cos\omega_0 t)\left( x_2 - i_{\alpha,ref} - x_1 + i_\alpha \right) \end{cases} \tag{14}$$

This article has been accepted for publication in a future issue of this journal, but has not been fully edited. Content may change prior to final publication. Citation information: DOI 10.1109/TPEL.2018.2867610, IEEE Transactions on Power Electronics

It is well known that $e_d$ and $e_q$ are both 0 in the steady-state condition. And then, it can be assumed that $dx_d/dt=e_d$ and $dx_q/dt=e_q$, where $x_d$ and $x_q$ are taken as two dummy state variables. Thus, the disturbance equations of $e_d$ and $e_q$ can be derived as (15) with the small disturbance:

$$\begin{cases} \dfrac{d\hat{x}_d}{dt} = \hat{e}_d = (\cos\omega_0 t)\left(\hat{i}_{\alpha,ref} - \hat{i}_\alpha\right) + (\sin\omega_0 t)\left(\hat{x}_2 - \hat{i}_{\alpha,ref} - \hat{x}_1 + \hat{i}_\alpha\right) \\ \dfrac{d\hat{x}_q}{dt} = \hat{e}_q = (\sin\omega_0 t)\left(\hat{i}_\alpha - \hat{i}_{\alpha,ref}\right) + (\cos\omega_0 t)\left(\hat{x}_2 - \hat{i}_{\alpha,ref} - \hat{x}_1 + \hat{i}_\alpha\right) \end{cases} \tag{15}$$

In addition, as shown in Fig. 1, since the same PI control and inverse Park's transformation are applied to $e_d$ and $e_q$, where PI=$k_p$+$k_i$/$s$, the reference of $i_c$ can be expressed as:

$$i_c^* = i_{c,\alpha}^* = (\cos\omega_0 t)\left(k_p e_d + k_i x_d\right) - (\sin\omega_0 t)\left(k_p e_q + k_i x_q\right) \tag{16}$$

Simplifying (16), the small-signal model of (16) can be derived as:

$$\hat{i}_c^* = k_p\left(\hat{i}_{\alpha,ref} - \hat{i}_\alpha\right) + k_i(\cos\omega_0 t)\hat{x}_d - k_i(\sin\omega_0 t)\hat{x}_q \tag{17}$$

where $k_p$ and $k_i$ represents the proportional and integral coefficient of the PI controller, respectively.

**Step 4:** Calculate the real modulation signal $u_{m,d}$. According to Fig. 1, after the proportional controller $K$ for the error signal of the inner current loop, $U_m$ can be derived as

$$U_m = K\left(i_c^* - i_c\right) \tag{18}$$

By applying the perturbation and linearization technique [39], the perturbation equation of (18) can be written as

$$\hat{u}_m = K\left(\hat{i}_c^* - \hat{i}_c\right) \tag{19}$$

Due to the hybrid modulation, the real modulation signal is $u_{m,d}$. According to the analysis given in Section II, the hybrid modulation can be approximated to $e^{-1.5sT_s}$. Therefore, $u_{m,d}$ can be obtained by applying $e^{-1.5sT_s}$ for $u_m$, which is the input of hybrid modulation under small disturbance condition.

By using the first-order Pade approximation [40], $e^{-1.5sT_s}$ can be denoted as:

$$e^{-1.5sT_s} \approx \frac{2-1.5sT_s}{2+1.5sT_s} \tag{20}$$

And then, a differential equation, including $u_m$ and $u_{m,d}$, can be derived as:

$$1.5T_s\frac{du_m}{dt} + 1.5T_s\frac{du_{m,d}}{dt} = 4u_m - 2\left(u_m + u_{m,d}\right) \tag{21}$$

It is assumed that $x_3$ is a new state variable and equal to $u_m$+$u_{m,d}$. And then, substituting $x_3$ into (21), and applying the perturbation and linearization technique [39], and the disturbed separation, we get:

$$\frac{d\hat{x}_3}{dt} = \frac{4}{1.5T_s}\hat{u}_m - \frac{2}{1.5T_s}\hat{x}_3 \tag{22}$$

**Step 5:** Derive the small-signal expression of the output signal $v_i$. According to the small-signal analysis of the hybrid modulation, there is a proportional loop in hybrid modulation $v_i$=$V_{dc}u_{m,d}$. Therefore, substituting (12), (13), (15), (17) and (19) into the (22), the perturbation equation of $v_i$ is written as

$$\hat{v}_i = V_{dc}\left(\hat{x}_3 - \hat{u}_m\right) = V_{dc}\cdot \left[\hat{x}_3 - Kk_p\hat{i}_{\alpha,ref} + Kk_p\hat{i}_g - Kk_i(\cos\omega_0 t)\hat{x}_d + Kk_i(\sin\omega_0 t)\hat{x}_q + K\hat{i}_c\right] \tag{23}$$

**Step 6:** Calculate the small-signal model of the ACHMI. According to (8), (12), (13), (15), (17), (19), (22) and (23), a differential equation based on the state variables with disturbance can be derived as

$$\frac{d\hat{\mathbf{X}}}{dt} = \mathbf{A}\hat{\mathbf{X}} + \mathbf{B}\hat{\mathbf{u}} \tag{24}$$

where, $\hat{\mathbf{X}} = \left[\hat{i}_g, \hat{v}_c, \hat{i}_c, \hat{x}_1, \hat{x}_2, \hat{x}_3, \hat{x}_d, \hat{x}_q\right]^T$, $\hat{\mathbf{u}} = \left[\hat{i}_{g,ref}, \hat{u}_{PCC}\right]^T$, and the expressions of **A** and **B** are listed in appendix A.

$$\hat{i}_g = \underbrace{\frac{m_0 s^5 + m_1 s^4 + m_2 s^3 + m_3 s^2 + m_4 s + m_5}{d_0 s^8 + d_1 s^7 + d_2 s^6 + d_3 s^5 + d_4 s^4 + d_5 s^3 + d_6 s^2 + d_7 s + d_8}}_{G_{c\_ig}(s)}\hat{i}_{gref} - \underbrace{\frac{n_0 s^7 + n_1 s^6 + n_2 s^5 + n_3 s^4 + n_4 s^3 + n_5 s^2 + n_6 s + n_7}{d_0 s^8 + d_1 s^7 + d_2 s^6 + d_3 s^5 + d_4 s^4 + d_5 s^3 + d_6 s^2 + d_7 s + d_8}}_{G_{a\_PLL}(s)}\hat{u}_{PCC} \tag{25}$$

Clearly, the ACHMI contains two input signals $i_{g,ref}$ and $u_{PCC}$, where $\hat{\imath}_{g,ref}$ and $\hat{u}_{PCC}$ are the small-signal component of $i_{g,ref}$ and $u_{PCC}$, respectively. The transfer function of each state variable and input signals with disturbance can be derived based on (24) by formula transformation and simplification. Thus, the small-signal model of the ACHMI can be derived as (25), where the coefficients $m_0$~$m_5$, $d_0$~$d_8$, $n_0$~$n_7$ are defined in appendix B. $G_{c\_ig}(s)$ represents the closed-loop transfer function of grid current, and $G_{a\_PLL}(s)$ denotes the output admittance of the ACHMI without PLL.

### *B. Small-Signal Model of PLL*

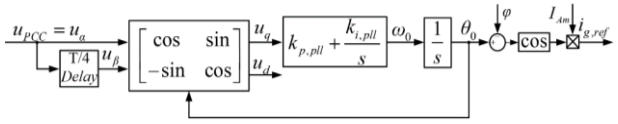


Fig. 6 Block diagram of the PLL [28-29], [36], [38].

For analyzing the effect of PLL on the grid-connected inverter, its mathematical model is required. Fig. 6 illustrates the block diagram of the SRF-PLL, where $u_{PCC}$ is taken as $u_\alpha$, the Park's transformation is applied to the phase detection and $u_q$ is controlled by PI controller for the phase tracking [41], [42]. By applying the perturbation and linearization technique [39], the linear model of the SRF-PLL can be expressed as:

$$\begin{cases} \hat{\theta}_0 = \int \hat{\omega}_0 dt \\ \hat{u}_q = -U_{m,d}\hat{\theta}_0 - \hat{u}_\alpha\sin\theta_0 + \hat{u}_\beta\cos\theta_0 \\ \hat{\omega}_0 = \left(k_{p,pll} + \int k_{i,pll}\right)\hat{u}_q \\ \hat{i}_{ref} \approx -I_{Am}\sin\left(\theta_0 - \varphi\right)\hat{\theta}_0 \end{cases} \tag{26}$$

where $U_{m,d}$ represents the peak PCC voltage, $I_{Am}$ denotes the peak value of current reference and $\varphi$ represents power angle.

By applying the Laplace transform to both sides of (26), considering $\hat{u}_\alpha$ is leading $\hat{u}_\beta$ by 90°, the transfer function of PLL can be written as (27), and the transfer function from the reference current $i_{g,ref}$ to $u_{PCC}$ can be expressed as (28).

$$G_{PLL}(s - j\omega_0) = \frac{1}{2}\cdot\frac{k_{p,pll}(s - j\omega_0) + k_{i,pll}}{(s - j\omega_0)^2 + U_{m,d}\left[k_{p,pll}(s - j\omega_0) + k_{i,pll}\right]} \tag{27}$$

$$\frac{\hat{i}_{g,ref}(s)}{\hat{u}_{PCC}(s)} = \frac{I_{Am}}{2}G_{PLL}(s - j\omega_0)\cdot e^{-j\varphi} \tag{28}$$

This article has been accepted for publication in a future issue of this journal, but has not been fully edited. Content may change prior to final publication. Citation information: DOI 10.1109/TPEL.2018.2867610, IEEE Transactions on Power Electronics

Furthermore, the small-signal model of PLL and the closed-loop transfer function of PLL can be derived as (29) and (30) respectively [41], [42].

$$T_{PLL}(s)=G_{PLL}(s-j\omega_0)\cdot e^{-j\varphi} \tag{29}$$

$$G_{c-PLL}=H_v I_{Am} T_{PLL}(s) \tag{30}$$

Finally, according to Fig. 1, Eq. (25) and Eq. (28), the complete small-signal model of the ACHMI with PLL can be derived as (31), which can be employed to derive the system impedance model.

$$\hat{i}_g(s)=G_{c\_ig}(s)I_{Am}H_v T_{PLL}\hat{u}_{PCC}(s)-G_{a\_PLL}(s)\hat{u}_{PCC}(s) \tag{31}$$

## IV. The Stability Analysis of the ACHMI under Weak Grid Condition

This section elaborates the stability analysis of the grid-connected ACHMI system under weak grid condition, where the grid impedance $Z_g$ cannot be neglected. With this condition, the grid-connected ACHMI and $Z_g$ can be regarded as a cascaded system for stability analysis, and then, the impedance-based stability criterion can be used for the stability analysis of the cascaded system [43]. However, with the classic stability criterion proposed in [43], the effect of PLL on the system stability is ignored. Hence, an improved impedance-based stability criterion with the PLL model is derived in this paper. With this criterion, the impact of the amplitude of the grid current ($I_{Am}$), the power factor angle ($\varphi$) and the bandwidth of PLL ($f_{BW}$) on the stability of the LCL-type single-phase grid-connected ACHMI can be analyzed.

### *A. The Derivation of the Stability Criteria*

Simplifying (31), the following expression can be obtained [42]:

$$i_g=-\frac{u_{PCC}}{Z_{PLL}}-\frac{u_{PCC}}{Z_i} \tag{32}$$

where the impedance of the PLL is represented by $Z_{PLL}$, which is written as (33).

$$Z_{PLL}=-\frac{1}{G_1(s)I_{Am}H_v T_{PLL}} \tag{33}$$

The output impedance $Z_i$ of the ACHMI without PLL introduced by the current loop can be expressed as:

$$Z_i=\frac{1}{G_2(s)} \tag{34}$$

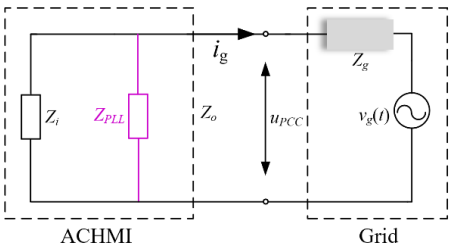


Fig. 7. Equivalent circuit of the grid-connected ACHMI with PLL.

According to Eq. (32) and voltage/current Kichhoff 's Laws, the equivalent circuit of the grid-connected ACHMI with PLL can be depicted in Fig. 7. It can be observed from Fig. 7 that the output impedance $Z_o$ of the ACHMI with PLL is equivalent to $Z_i$ in parallel with the negative impedance $Z_{PLL}$ [42], which can be written as

$$Z_o=\frac{Z_i\cdot Z_{PLL}}{Z_i+Z_{PLL}} \tag{35}$$

According to the equivalent circuit, as shown in Fig. 7, the grid current $i_g$ can be expressed as

$$i_g=-\frac{v_g}{Z_o}\cdot\frac{1}{1+Z_g/Z_o} \tag{36}$$

For a stable grid-connected ACHMI system, the following two conditions can be formulated based on the Eq.(36).

(i) The $1/Z_o$ is stable when supplied by an ideal grid voltage.

(ii) The ratio of the impedance $Z_g$ to the impedance $Z_o$ satisfies the Nyquist criterion [43].

In view of (i), when $1/Z_o$ is stable, the system is stable under ideal grid voltage condition. According to Fig. 7, $Z_o$ is obtained by $Z_{PLL}$ in parallel with $Z_i$, which is written as (35). Clearly, the poles of $1/Z_o$ are the same as the poles of $1/Z_{PLL}$ plus the poles of $1/Z_i$. Therefore, when both $1/Z_{PLL}$ and $1/Z_i$ are stable, the stability of $1/Z_o$ can be guaranteed.

Comparing (25) and (34), it can be seen that $1/Z_i$ has the same poles with the closed-loop transfer function $G_{c\_ig}(s)$ of the grid current. Namely, $1/Z_i$ and $G_{c\_ig}(s)$ have the same stability characteristics based on the Root Locus based stability evaluation scheme. Hence, the stability of $1/Z_i$ can be guaranteed when the grid current closed-loop is stable. Besides, by comparing (33) and (30), it can be observed that the poles of $1/Z_{PLL}$ are the poles of $G_{c\_g}(s)$ plus the poles of closed-loop transfer function $G_{c\text{-}PLL}(s)$ of PLL. Therefore, when the stability of both the current loop and the closed-loop of PLL can be guaranteed, $1/Z_{PLL}$ is stable.

As a result, $1/Z_o$ would be stable when the stability of the current loop and the closed-loop of PLL can be guaranteed simultaneously. Since the scenario (i) is equivalent to the strong grid condition, the grid impedance can be approximated to zero. And then, $u_{PCC}$ is equal to $v_g$ and Eq. (36) can be rewritten as $i_g=-v_g/Z_o$. With this scenario, the condition (ii) can be ignored and the stability requirement of the grid-connected ACHMI is to make sure that the closed-loop grid current control and PLL are both stable.

In view of (ii), the grid impedance $Z_g$ is considered and the ACHMI system operates under a weak grid condition. With this condition, in order to achieve a good robustness and dynamic response, the phase margin (PM) of $Z_g/Z_o$ should be in the range of [30°, 60°] at their crossover frequency $f_{cg\_o}$, where PM can be expressed as:

$$\mathrm{PM}=180^\circ+\angle\left(Z_o(s)-Z_g(s)\right)\Big|_{s=j2\pi f_{cg\_o}} \tag{37}$$

In most of the industrial applications, the line impedance and grid impedance $Z_g$ are highly inductive. In that case, the phase of $Z_g$ is almost 90°, and then, Eq. (37) can be rewritten as:

$$\mathrm{PM}=90^\circ+\angle Z_o(s)\Big|_{s=j2\pi f_{cg\_o}} \tag{38}$$

According to (38), in order to guarantee the condition 30°≤PM≤60°, the phase of $Z_o$ should be in the range of [-60°, -30°]. However, the negative factor provided by $Z_{PLL}$ is introduced into $Z_o$, which has negative influence on the stability of ACHMI. Hence, it is necessary to analyze the effects of PLL on $Z_o$.

### *B. The Effect of PLL on $Z_o$*

According to (34) and (35), the bode diagrams of $Z_i$, $Z_o$ and different $Z_g$ can be depicted, as shown in Fig. 8. $Z_o$ is obtained by $Z_i$ in parallel with $Z_{PLL}$, where $Z_{PLL}$ is the negative impedance as analyzed earlier. Thus, the phase of $Z_o$ is diminished at the crossover frequency $f_{cg\_o}$ of $Z_g$ and $Z_o$ due to the effect of $Z_{PLL}$, as shown in Fig. 8, which results in the decrease of PM. In addition, the value of PM is different with different $Z_g$, and PM gradually

This article has been accepted for publication in a future issue of this journal, but has not been fully edited. Content may change prior to final publication. Citation information: DOI 10.1109/TPEL.2018.2867610, IEEE Transactions on Power Electronics

increases with the decrease of $Z_g$. Thus, it can be found that the grid impedance has influences on the stability of the ACHMI system. Obviously, with the same $Z_g$, the phase at the crossover frequency $f_{cg\_on}$ ($n$=1, 2, 3) of $Z_o$ and $Z_g$ is smaller than the phase at the crossover frequency $f_{cg\_in}$ ($n$=1, 2, 3) of $Z_i$ and $Z_g$, and the phase margin and system stability at $f_{cg\_on}$ ($n$=1, 2, 3) is worse than the phase margin and system stability at $f_{cg\_in}$ ($n$=1, 2, 3), which reveals that the PLL has effects on the system stability. Hence, it is necessary to perform a thorough analysis about the effects of PLL on $Z_o$. From (33), only $I_{Am}$, $1/G_{PLL}$ and power factor angle $\varphi$ have impact on the performance of $Z_{PLL}$ and other variables are determined by current loop. Thus, the analysis about the effects of PLL on $Z_o$ is equivalent to the analysis on the influences of $I_{Am}$, $1/G_{PLL}$ and $\varphi$ on $Z_o$.

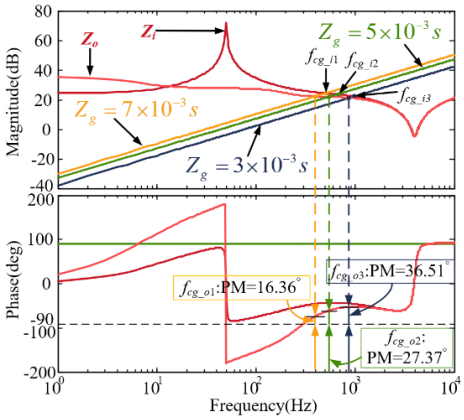


Fig. 8. Bode diagrams of $Z_i$, $Z_o$ and different $Z_g$.

### *B*.1. *Power Factor Angle φ*

Fig. 9 illustrates the bode diagrams of $Z_o$ with different $\varphi$. $Z_o$ is obtained by $Z_i$ in parallel with $Z_{PLL}$, thus, the different $\varphi$ has impact on $Z_o$ as shown in the aforementioned analysis. In Fig. 9, it can be seen that the different phase of $Z_o$ is caused by different values of $\varphi$. Moreover, when $\varphi$ is within [-90°, 90°], the changing of the phase of $Z_o$ is not monotonous with the changing of $\varphi$. Thus, $\varphi$ should be considered when analyzing the effects of PLL on $Z_o$. It is well known that the grid-connected inverter often works on three typical operating conditions, namely, $\varphi$=0°, $\varphi$=90° and $\varphi$=-90°. From Fig. 9, it can be observed that the PM is lowest when $\varphi$=-90°. Therefore, the subsequent parameter design procedure is presented based on the condition $\varphi$=-90°, which is validated by the extensive simulation and experimental results under the three conditions.

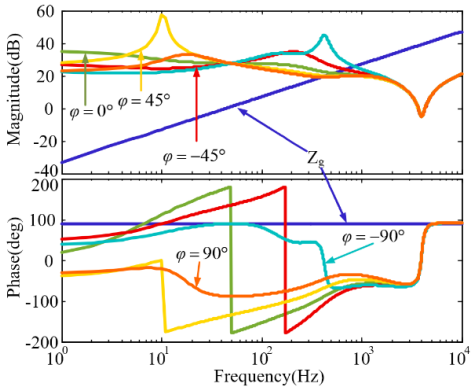


Fig. 9 Bode diagrams of impedance $Z_o$ with different power factor angle $\varphi$.

### *B*.2. *Reference Current Amplitude* $I_{Am}$

Fig. 10 illustrates the bode diagrams of $Z_o$ with different reference current amplitude $I_{Am}$. $Z_o$ is obtained by $Z_i$ in parallel with $Z_{PLL}$, thus, the different $I_{Am}$ has impact on $Z_o$ as the aforementioned analysis. In Fig. 10, it can be observed that the larger $I_{Am}$ leads to a smaller PM of $Z_g/Z_o$ at the crossover frequency $f_{cg\_o}$, and the stability margin of ACHMI is reduced with a larger $I_{Am}$. Moreover, PM is sensitive to $I_{Am}$ since a small change of $I_{Am}$ results in a large variation of PLL.

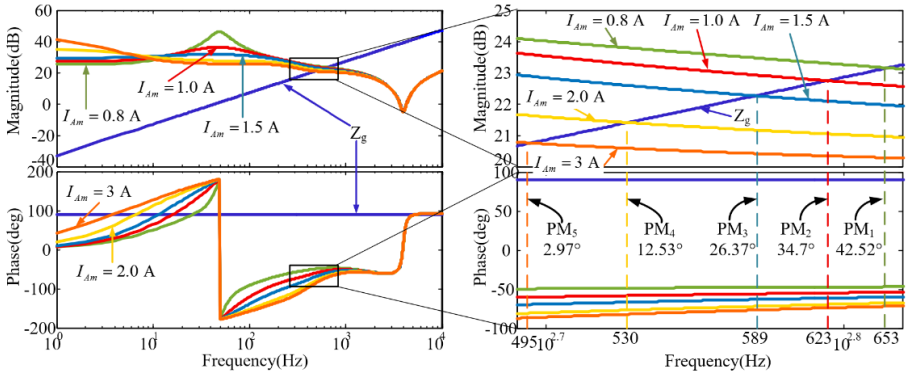


Fig. 10 Bode diagrams of impedance $Z_o$ with different reference current amplitude $I_{Am}$.

### *B*.3. *Bandwidth of PLL* $f_{BW}$

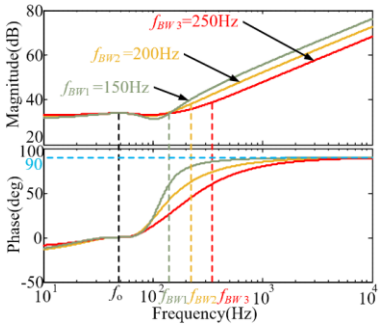


Fig. 11 Bode diagrams of $1/G_{PLL}$ with different bandwidth $f_{BW}$.

The characteristics of $G_{PLL}$ can be obtained according to Eq. (27), which shows the same characteristics with the low pass filter above the fundamental frequency $f_0$. The bode diagrams of $1/G_{PLL}$ with different $f_{BW}$ are depicted in Fig. 11. From Fig. 11, it can be observed that the phase frequency curve of $1/G_{PLL}$ has a 0°~90° phase shift when $f>f_o$, and the magnitude increases with the increase of frequency when $f>f_{BW}$. In the high frequency range, the amplitude and phase angle of $1/G_{PLL}$ would decreases with an increase of $f_{BW}$, thus, the amplitude and phase angle of $Z_o$ also decreases, which leads to a lower phase margin (PM) of ACHMI.

In conclusion, power factor angle $\varphi$, reference current amplitude $I_{Am}$ and bandwidth $f_{BW}$ of the $G_{PLL}$ may cause negative influence on $Z_o$ through $Z_{PLL}$, which result in the decrease of the stability margin for the grid-connected ACHMI. Therefore, the design of $f_{BW}$ is crucial for the performance of the grid-connected ACHMI system. Since the different control parameters of PLL has different $f_{BW}$, the control parameter design can be simplified as the selection of $f_{BW}$.

## *C. Parameter Design*

This article has been accepted for publication in a future issue of this journal, but has not been fully edited. Content may change prior to final publication. Citation information: DOI 10.1109/TPEL.2018.2867610, IEEE Transactions on Power Electronics

This section focuses on the parameter design of PLL and how to select reference current amplitude $I_{Am}$. In view of the Eq. (27), it is assumed that $2\zeta\omega_n = U_m k_{p,pll}$ and $\omega_n^2 = U_m k_{i,pll}$. Referring to [44], the PLL can maintain a good stability and dynamic response when $\zeta$=0.707. According to the definition of $f_{BW}$, the following expression can be derived as (39), presented at the bottom of the page.

Based on (39), the control parameters $k_{p,pll}$ and $k_{i,pll}$ of PLL can be written as

$$\begin{cases} k_{p,pll} = \dfrac{4\xi\pi f_{BW} - 2\xi\omega_0}{U_m\sqrt{\sqrt{2+4\xi^2+4\xi^4}+1+2\xi^2}} \\ k_{i,pll} = \dfrac{\left(2\pi f_{BW} - \omega_0\right)^2}{U_m\left(\sqrt{2+4\xi^2+4\xi^4}+1+2\xi^2\right)} \end{cases} \tag{40}$$

According to (40), the graph of $k_{p,pll}$ and $k_{i,pll}$ with the variation of $f_{BW}$ can be depicted, as shown in Fig. 12. In Fig. 12, it can be seen that different $k_{p,pll}$ and $k_{i,pll}$ can be obtained with different $f_{BW}$. Moreover, $f_{BW}$ has a monotonous variation with $k_{p,pll}$ and $k_{i,pll}$, respectively. Hence, it can be found that $f_{BW}$ has significant impact on the stability and dynamic performance of PLL through the control parameters $k_{p,pll}$ and $k_{i,pll}$ of PLL.

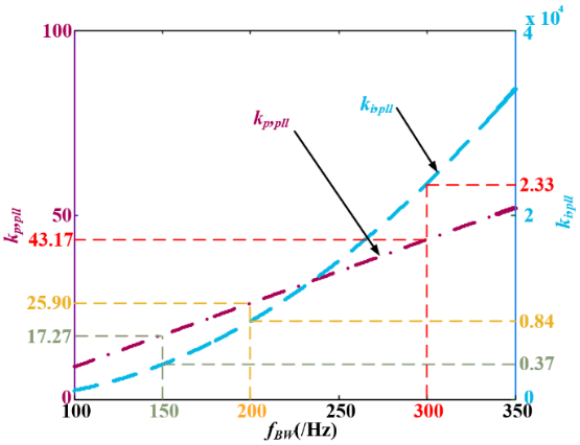


Fig. 12 The values of $k_{p,pll}$ and $k_{i,pll}$ with different $f_{BW}$.

Substituting (35) and (40) into (38), the expression of PM can be rewritten as (41), presented at the bottom of the page, where the parameter $G_{PM1}$ and $G_{PM2}$ is denotes as $2G_{a\_PLL}(s)U_{m,d}(s\text{-}j\omega_0)$ and $G_{c\_ig}(s)I_{Am}H_v(s\text{-}j\omega_0)e^{-j\varphi}$, respectively.

According to (41) and the parameters listed in TABLE I, the PM, $f_{BW}$ and $I_{Am}$ can be represented in 3-D plots shown in Fig. 13, where the parameters $k_p$, $k_i$ and $K$ of current controller are determined experimentally. Therefore, the PM can satisfy the range [30°, 60°] as long as $f_{BW}$ and $I_{Am}$ are properly selected. In Fig. 13, it can be observed that the excessive increase of $f_{BW}$ may lead to a negative PM and the system tends to be unstable. And, the PM would also be decreased with an increase of $I_{Am}$ under a fixed $f_{BW}$. From Fig. 13, the grid-connected ACHMI system is in a critical state in the case of $f_{BW}$=143Hz and $I_{Am}$=0.5A, where the phase margin (PM) is 30°, and the decrease of $f_{BW}$ will result in a positive PM in this case, which would improve the stability of ACHMI system. In addition, the studied ACHMI system tends to be unstable in the case of $f_{BW}$=143Hz and $I_{Am}$=2.3A, where the phase margin PM is 19°. And, the PM can be increased with a decrease of $f_{BW}$ under this parameter condition, which would improves the stability of ACHMI system. Form Fig. 13, when $f_{BW}$ is equal to126Hz, it can be observed that the value of PM in case of $I_{Am}$=2.3A and $I_{Am}$=0.5A is 32.6° and 53.8°, respectively. Therefore, the maximum value of $f_{BW}$ is 126Hz when the reference $I_{Am}$ is in the range of [0.3A, 2.3A]. Notably, the value of $f_{BW}$ can be changed with different range of $I_{Am}$, the parameter design method presented in this section can also be adopted to select $f_{BW}$. Finally, the corresponding simulation and experimental results are provided in Section V and VI, respectively.

TABLE I. PARAMETERS OF ASYMMETRICAL CASCADED H-BRIDGE MULTILEVEL INVERTER SYSTEM

| Parameters | Symbol | Values |
|---|---|---|
| DC Voltage | $V_{dc1}$, $V_{dc2}$, $V_{dc3}$ | 3V, 6V, 18V |
| Peak Grid Voltage | $U_{m,d}$ | 23V |
| Fundamental frequency | $f_0$ | 50Hz |
| LCL Filter | $L_1$ | 1.8mH |
| | $C$ | 2.2μF |
| | $L_2$ | 1.2mH |
| Sampling Period | $T_s$ | 0.1ms |
| Current Controller | $K$ | 0.8 |
| | $k_p$ | 0.03 |
| | $k_i$ | 20 |
| PLL-bandwidth | $f_{BW}$ | (100~400)Hz |
| Peak value of reference | $I_{Am}$ | (0.3~3.7)A |

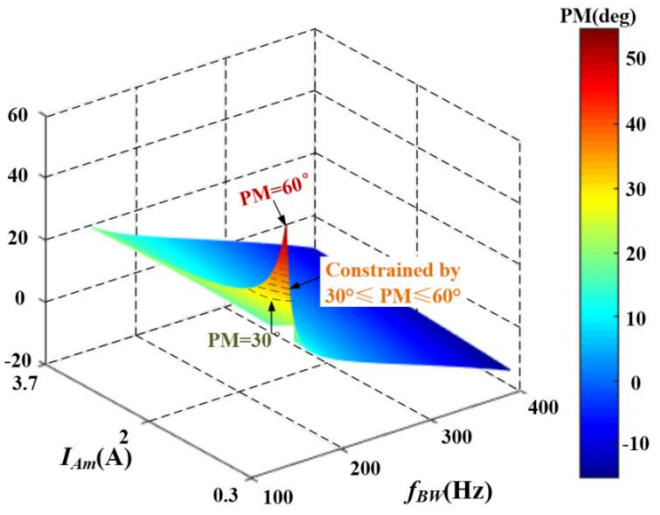


Fig. 13 The PM, $I_{Am}$ and $f_{BW}$ of ACHMI with the effect of PLL.

$$\left|G_{PLL}\left(j\omega_0 + j2\pi f_{BW}\right)\right| = \left|\frac{1}{2U_{m,d}} \cdot \frac{2\xi\omega_n\left(j\omega_0 + j2\pi f_{BW}\right) + \omega_n^2}{\left(j\omega_0 + j2\pi f_{BW}\right)^2 + 2\xi\omega_n\left(j\omega_0 + j2\pi f_{BW}\right) + \omega_n^2}\right| = 1 \tag{39}$$

$$\mathrm{PM} = 90^\circ + \angle\left\{\frac{8.46\left(4\pi f_{BW}\xi - 2\omega_0\xi\right)\left(s - j\omega_0\right) + 4.12\left(2\pi f_{BW} - \omega_0\right)^2 + 17.43\left(s - j\omega_0\right)^2}{4.23\left(4\pi f_{BW}\xi - 2\omega_0\xi\right)\left[G_{PM1} - G_{PM2}\right] + 2.06\left(2\pi f_{BW} - \omega_0\right)^2\left[2G_{a\_\_PLL}(s)U_{m,d} + G_{c\_ig}(s)I_{Am}H_v e^{-j\varphi}\right] + 17.43G_{a\_\_PLL}(s)\left(s - j\omega_0\right)^2 U_{m,d}}\right\}\Bigg|_{s=j2\pi f_{cg\_o}} \tag{41}$$

This article has been accepted for publication in a future issue of this journal, but has not been fully edited. Content may change prior to final publication. Citation information: DOI 10.1109/TPEL.2018.2867610, IEEE Transactions on Power Electronics

## V. Simulation Results

To evaluate the effectiveness of the dual-loop current control strategy built in the hybrid reference frame, hybrid modulation method, and the stability analysis, the time-domain simulations using the MATLAB/Simulink are carried out. The main circuit and current controller parameters are given in Table I.

Fig. 14 shows the steady-state waveforms of the single-phase ACHMI under strong grid condition, where grid impedance is approximately 2.4mH, $I_{Am}$=0.5A and $f_{BW}$ is 126Hz. According to (40), the value of $k_{p,pll}$ and $k_{i,pll}$ can be obtained, which is 13.12 and 2153.5, respectively. The simulation waveforms tested with $f_{BW}$=126Hz and $f_{BW}$=600Hz are shown in Fig. 14(a) and Fig. 14(b), respectively. It can be observed that the $i_g$ depicted in Fig. 14(a) and Fig. 14(b) is periodic and almost sinusoidal without any distortion, and Fig. 14(b) is almost the same as the case in Fig. 14(a), which indicates the grid-connected ACHMI system is stable and the system can also be stable with different values of $f_{BW}$.

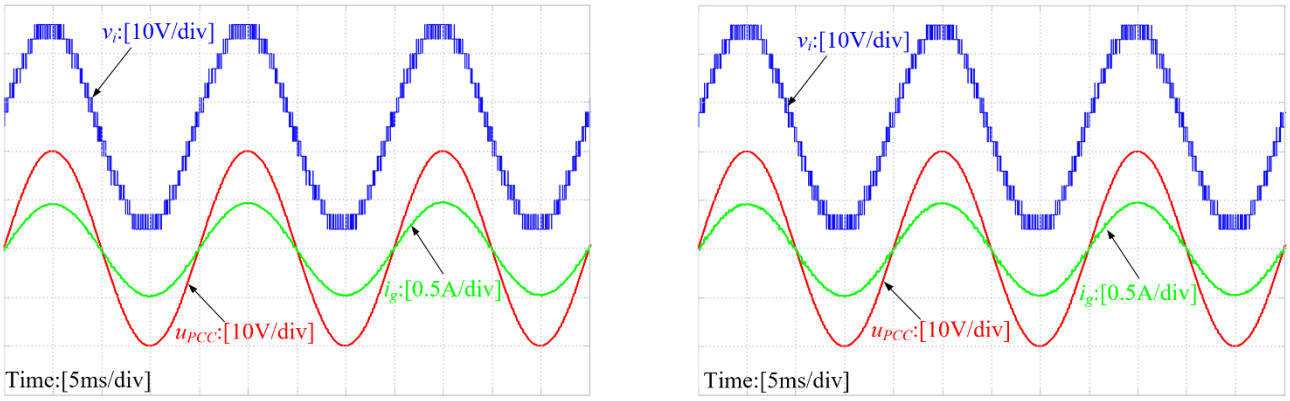


(a) $f_{BW}$=126Hz (b) $f_{BW}$=600Hz

Fig. 14 Simulation results of the grid-connected single-phase ACHMI under strong grid condition.

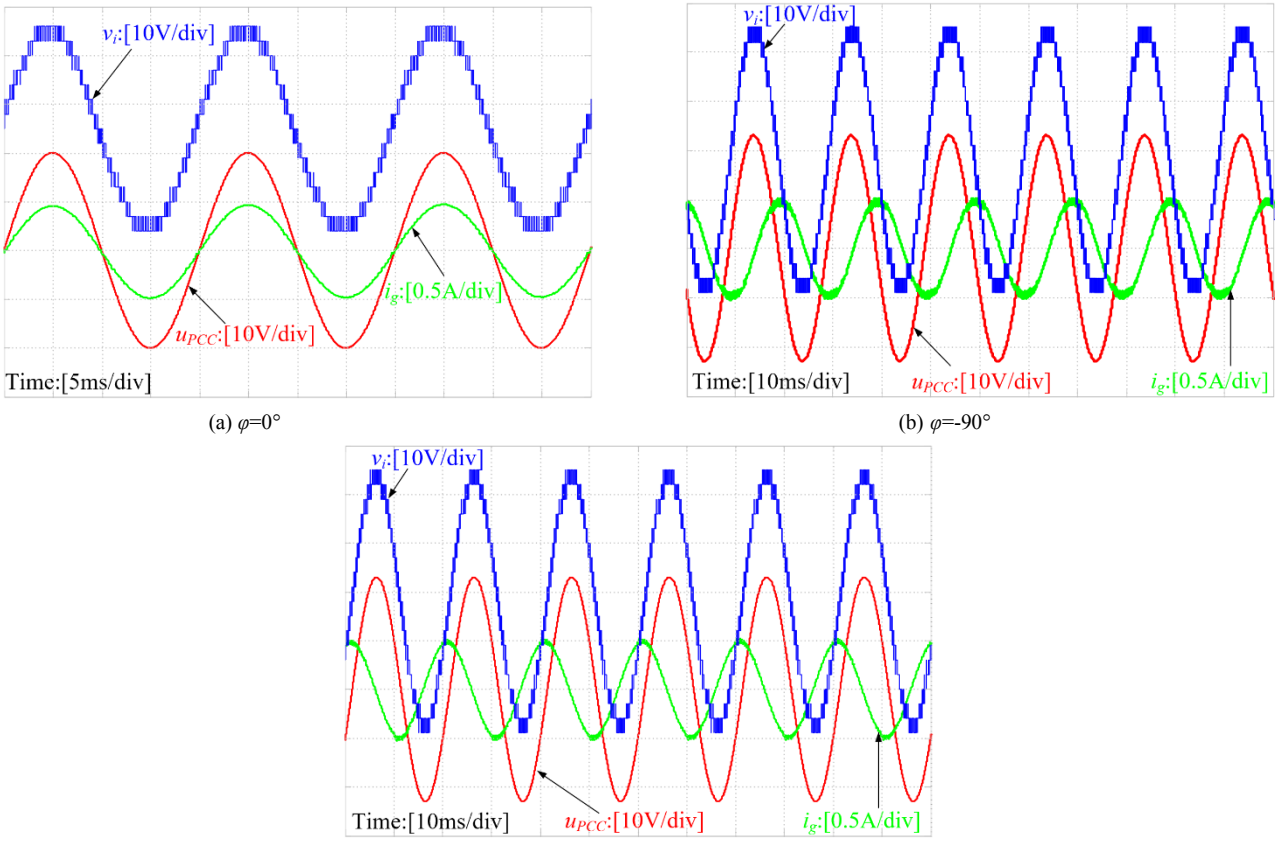


(a) $\varphi$=0° (b) $\varphi$=-90°

(c) $\varphi$=90°

Fig. 15 Simulation results of the grid-connected single-phase ACHMI in case of weak grid condition under different $\varphi$.

Fig. 15 illustrates the steady-state waveforms of the ACHMI system under weak grid condition, where grid impedance is approximately 0.6mH and $I_{Am}$=0.5A. The simulation waveforms tested with $f_{BW}$=126Hz and $f_{BW}$=600Hz are shown in Fig. 14(a) and Fig. 14(b), respectively. It can be observed that the $i_g$ depicted in Fig. 14(a) and Fig. 14(b) is periodic and almost sinusoidal without any distortion, and Fig. 14(b) is almost the same as the case in Fig. 14(a), which indicates the grid-connected ACHMI system is stable and the system can also be stable with different values of $f_{BW}$.

Fig. 15 illustrates the steady-state waveforms of the ACHMI system under weak grid condition, where grid impedance is approximately 2.4mH, $I_{Am}$=0.5A and $f_{BW}$ is 126Hz. According to (40), the value of $k_{p,pll}$ and $k_{i,pll}$ can be obtained, which is 13.12 and 2153.5, respectively. The simulation waveforms tested with $\varphi$=0°, $\varphi$=-90° and 90°are shown in Fig. 15(a), Fig. 15(b) and Fig. 15(c), respectively. It can be seen that the $i_g$ is periodic and sinusoidal without any distortion, which indicates the grid-connected ACHMI system is stable under three different $\varphi$ and each PM of the three conditions both satisfies the range of [30°, 60°] based on the designed parameters.

Fig. 16 illustrates the transient waveforms of the ACHMI system under weak grid condition, where grid impedance is approximately 2.4mH and $f_{BW}$ is 126Hz. And according to (40), the value of $k_{p,pll}$ and $k_{i,pll}$ can be obtained, which is 13.12 and 2153.5, respectively. The transient simulation waveforms tested with $\varphi$=-90° and 90°are shown in Fig. 16(a) and Fig. 16(b) respectively, where the dynamic response of the grid-connected ACHMI system in case of $\varphi$=-90° and $\varphi$=90° are both tested when $I_{Am}$ jumps from 0.5A to 1A at the step point. Clearly, $i_g$ remains periodic and sinusoidal without any distortion when the step increase of $I_{Am}$ is applied. Moreover, the response time is 0.24ms when $\varphi$=-90° and the response time is 0.20ms when $\varphi$=90°, which shows a fast dynamic response with adopted dual-loop current control method.

As shown in Fig. 17, the dynamic response of the ACHMI

This article has been accepted for publication in a future issue of this journal, but has not been fully edited. Content may change prior to final publication. Citation information: DOI 10.1109/TPEL.2018.2867610, IEEE Transactions on Power Electronics

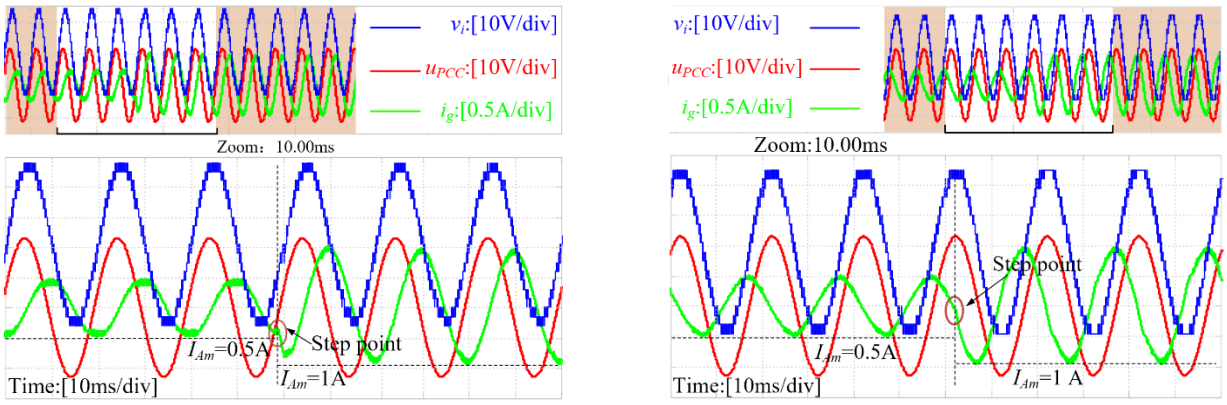


(a) $\varphi$=-90° (b) $\varphi$=90°

Fig. 16 The transient simulation waveforms of the grid-connected single-phase ACHMI under different $\varphi$.

system under weak grid condition from $\varphi$=-90° to $\varphi$=90° has been simulated, where grid impedance is approximately 2.4mH and $f_{BW}$ is 126Hz. In this case, the reference current $i_{g,ref}$ changes from $I_{Am}\sin(\theta_0$-90°) to $I_{Am}\sin(\theta_0$+90°) at the step point and $I_{Am}$=0.5A. Besides, the control parameters are consistent with the initial settings. It can be seen that the $i_g$ depicted in Fig. 17 can also maintain periodic and sinusoidal without any distortion after the step point, and the response time is 0.4ms. Therefore, the waveforms depicted in Fig. 17 further show a fast dynamic response for the the studied system with adopted dual-loop current control method.

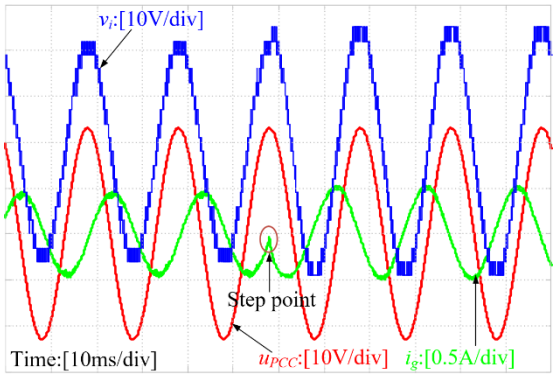


Fig. 17 The simulation waveforms of the grid-connected single-phase ACHMI under the transition from $\varphi$=-90° to $\varphi$=90°.

Fig. 18 illustrates the simulation waveforms of the grid-connected ACHMI under weak grid condition, where the grid impedance is also set as 1.8mH and $f_{BW}$ is set as 200Hz. According to (40), the value of $k_{p,pll}$ and $k_{i,pll}$ can be obtained, which is 25.90 and 8388.8, respectively. As shown in Fig. 18, the waveforms of $u_{PCC}$, $v_i$ and $i_g$ show a slight oscillation with the selected $f_{BW}$. Compared to Fig. 15(a), it is obvious that the oscillation of the simulation waveforms is caused by the increase of $f_{BW}$ under weak grid condition. Moreover, if $f_{BW}$ continue to be enlarged, the oscillation can be aggravated, which may lead to instability of the grid-connected ACHMI system.

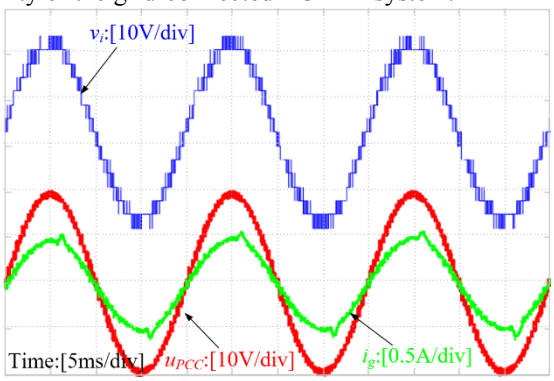


Fig. 18 The simulation waveforms of the grid-connected single-phase ACHMI under weak grid condition with $f_{BW}$=200Hz.

## VI. Experimental Results

A downscaled LCL-type single-phase grid-connected ACHMI is set up, where the hardware system consists of three full-bridge power modules, an LCL filter, voltage sensor HPT205A and current sensor ACS712ELCTR-05B-T. The control algorithm is implemented in TMS320F28335 DSP, and the DC-link voltage of the ACHMI is provided by three programmable DC power supplies. In addition, the grid impedance is emulated by connecting a stepdown transformer with an additional 1.8mH inductance between the strong grid and ACHMI, where the leakage inductance of the transformer is approximately 0.6mH. In order to provide effective comparison, all the control parameters are consistent with simulation.

To verify the simulation case studies, Fig. 19 shows the measured steady-state waveforms of the ACHMI under strong grid condition, where the grid impedance is approximately 0.6mH and $I_{Am}$=0.5A. The experimental waveforms tested with

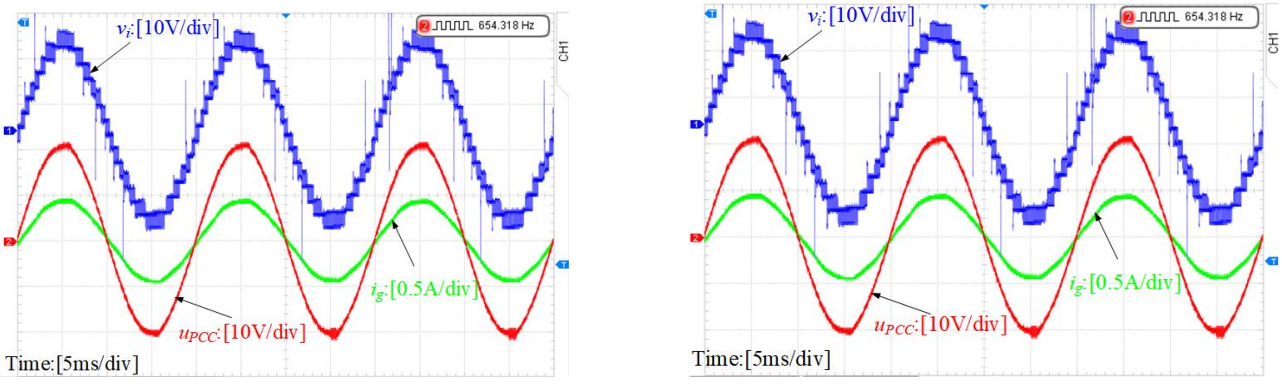


(a) $f_{BW}$=126Hz (b) $f_{BW}$=600Hz

Fig. 19 The experimental results of the grid-connected single-phase ACHMI under strong grid condition.

This article has been accepted for publication in a future issue of this journal, but has not been fully edited. Content may change prior to final publication. Citation information: DOI 10.1109/TPEL.2018.2867610, IEEE Transactions on Power Electronics

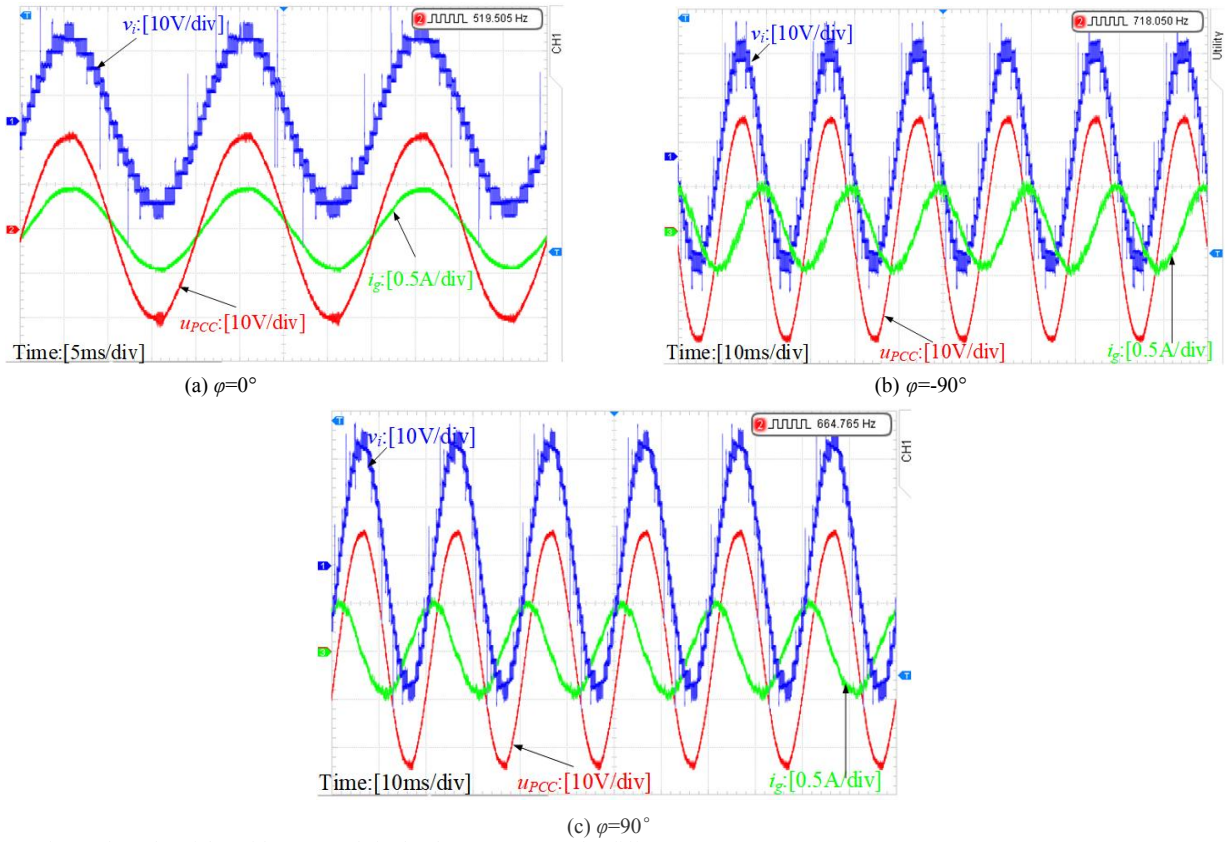


(a) $\varphi$=0° (b) $\varphi$=-90°

(c) $\varphi$=90°

Fig. 20 The experimental results of the grid-connected single-phase ACHMI under different $\varphi$.

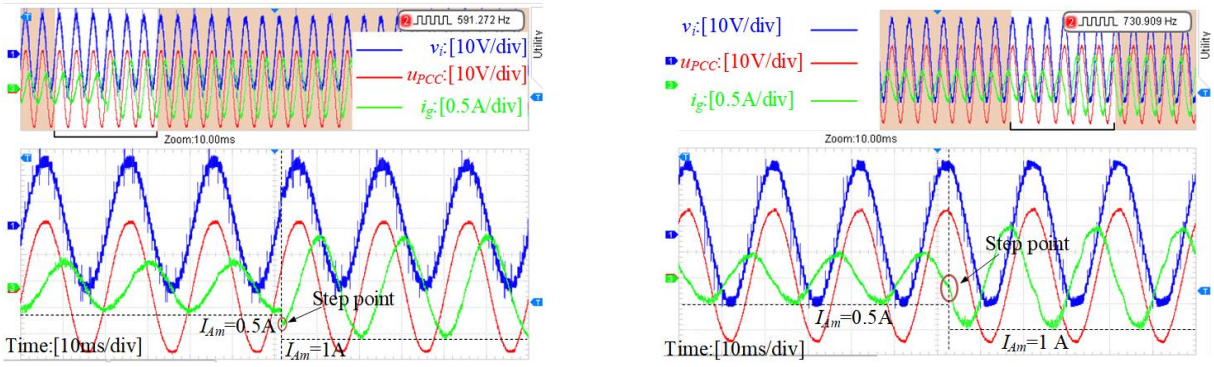


(a) $\varphi$=-90° (b) $\varphi$=90°

Fig. 21 The transient experimental waveforms of the grid-connected single-phase ACHMI under different $\varphi$.

$f_{BW}$=126Hz and $f_{BW}$=600Hz are shown in Fig. 19(a) and Fig. 19(b), respectively. It can be seen that the experimental waveforms match with the simulation results in Fig. 14. Thus, the conclusion mentioned in Section IV, that the ACHMI is stable as long as the stability of grid current and PLL closed-loop can be guaranteed respectively under strong grid condition, has been verified by the simulation and experimental results.

Fig. 20 shows the measured steady-state waveforms for the ACHMI system under weak grid condition. The experimental waveforms tested with $\varphi$=0°, $\varphi$=-90° and 90°are shown in Fig. 20(a), Fig. 20(b) and Fig. 20(c), respectively. It agrees with the simulation results in Fig. 15. Therefore, the condition (ii) mentioned in Section IV(A) and the parameter design explained in Section IV(C) are validated by the simulation and experimental results.

Fig. 21 provides the dynamic waveforms for ACHMI system with $\varphi$=-90° and 90°, where a fast dynamic response is observed. The tested results under the same variation of $\varphi$ as the simulation study is given in Fig. 22. A close related to the simulation results shown in Fig. 16 and Fig. 17 can be observed in both cases. As a result, the effectiveness of the parameter design and selection method mentioned in Section IV(C) is verified by the dynamic simulation and experimental results.

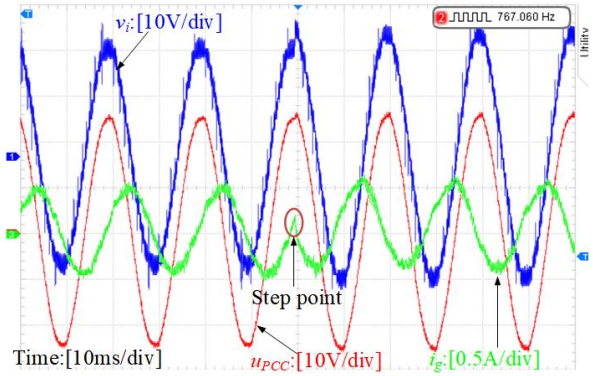


Fig. 22 The experimental waveforms of the grid-connected single-phase ACHMI under the transition from $\varphi$=-90° to $\varphi$=90°.

Fig. 23 shows the measured waveforms for the proposed parameters design scheme with the studied $f_{BW}$. Similar to the simulation results shown in Fig. 18, there is slight oscillation on the tested waveforms with the selected $f_{BW}$. Compared to Fig. 20(a), it also can been seen that the oscillation of the experimental waveforms is caused by the increase of $f_{BW}$ under weak grid scenarios. Therefore, the simulation and experimental results show a good consistency with the parameter design approach mentioned in Section IV(C).

This article has been accepted for publication in a future issue of this journal, but has not been fully edited. Content may change prior to final publication. Citation information: DOI 10.1109/TPEL.2018.2867610, IEEE Transactions on Power Electronics

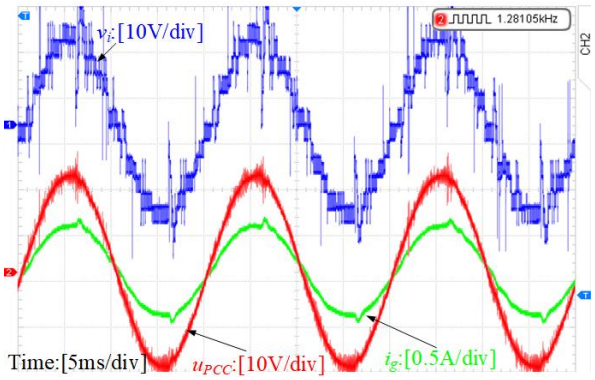


Fig. 23 The experimental waveforms of the grid-connected single-phase ACHMI under weak grid condition with $f_{BW}$=200Hz.

## VII. Conclusion

This paper discussed the effect of PLL on the stability of the LCL-type single-phase grid-connected ACHMI under weak grid scenarios, where the adopted dual-loop current control scheme established in hybrid reference frame, and the hybrid modulation method are considered simultaneously. For the integrity of the stability analysis, the complete small-signal model of the ACHMI, including the power-stage and control system, is established by a simple step-by-step derivation method. And then, a system impedance model is built based on the derived small-signal model of ACHMI, and an improved impedance stability criterion is adopted to determine the system stability. With this criterion, it can be obtained that the ACHMI is stable when both the grid current loop and PLL loop are stable under the strong grid condition, and a larger value of the bandwidth $f_{BW}$ of the PLL reduces the stability margin of the ACHMI under weak grid scenarios. Moreover, reference current $I_{Am}$ also has an impact on the stability of ACHMI under weak grid scenario. In addition, a simplified design method for controller parameters of PLL is proposed to improve the performance of the steady-state and dynamic response by using theoretical analysis. Finally, a reduced-size laboratory prototype LCL-type single-phase grid-connected ACHMI is built to confirm the validity and effectiveness of the theoretical analysis.

## Appendix A

Expression of **A** and **B** in Equation (24):

$$\mathbf{A}=\begin{bmatrix}
0 & \frac{1}{L_2} & 0 & 0 & 0 & 0 & 0 & 0\\
0 & 0 & \frac{1}{C} & 0 & 0 & 0 & 0 & 0\\
\frac{V_{dc}k_pK}{L_1} & -\frac{1}{L_1}-\frac{1}{L_2} & \frac{V_{dc}K}{L_1} & 0 & 0 & \frac{V_{dc}}{L_1} & -\frac{V_{dc}Kk_i}{L_1}\cos\omega_0 t & \frac{V_{dc}Kk_i}{L_1}\sin\omega_0 t\\
\frac{4}{\tau} & 0 & 0 & -\frac{2}{\tau} & 0 & 0 & 0 & 0\\
0 & 0 & 0 & 0 & -\frac{2}{\tau} & 0 & 0 & 0\\
\frac{4Kk_p}{1.5T_s} & 0 & -\frac{4K}{1.5T_s} & 0 & 0 & -\frac{2K}{1.5T_s} & \frac{4Kk_i\cos\omega_0 t}{1.5T_s} & -\frac{4Kk_i\sin\omega_0 t}{1.5T_s}\\
\sin\omega_0 t-\cos\omega_0 t & 0 & 0 & -\sin\omega_0 t & \sin\omega_0 t & 0 & 0 & 0\\
\sin\omega_0 t+\cos\omega_0 t & 0 & 0 & -\cos\omega_0 t & \cos\omega_0 t & 0 & 0 & 0
\end{bmatrix} \tag{A1}$$

$$\mathbf{B}=\begin{bmatrix}
0 & 0 & -\frac{V_{dc}k_pK}{L_1} & 0 & \frac{4}{\tau} & \frac{4Kk_p}{1.5T_s} & \cos\omega_0 t-\sin\omega_0 t & -(\cos\omega_0 t+\sin\omega_0 t)\\
-\frac{1}{L_2} & 0 & 0 & 0 & 0 & 0 & 0 & 0
\end{bmatrix}^T \tag{A2}$$

## Appendix B

Definitions of Coefficients in Equation (25):

| | | |
|---|---|---|
| $m_0=1.5T_sa_0KV_{dc}$ | $m_1=2a_0KV_{dc}+1.5T_sa_1KV_{dc}$ | $m_2=2a_1KV_{dc}+1.5T_sa_2KV_{dc}$ |
| $m_3=2a_2KV_{dc}+1.5T_sa_3KV_{dc}$ | $m_4=2a_3KV_{dc}+1.5T_sa_4KV_{dc}$ | $m_5=2a_4KV_{dc}$ |
| $d_0=e_0b_0$ | $d_1=e_0b_1+e_1b_0$ | $d_2=e_0b_2+e_1b_1+e_2b_0$ |
| $d_3=e_0b_3+e_1b_2+e_2b_1+e_3b_0+m_0$ | $d_4=e_0b_4+e_1b_3+e_2b_2+e_3b+m_1$ | $d_5=e_1b_4+e_2b_3+e_3b_2+m_2$ |
| $d_6=e_2b_4+e_3b_3+m_3$ | $d_7=e_3b_4+m_4$ | $d_8=m_5$ |
| $n_0=1.5T_sCL_1b_0$ | $n_1=b_0(2CL_1-1.5T_sCL_1KV_{dc})+1.5T_sCL_1b_1$ | |
| $n_2=b_0(1.5T_s+2CL_1KV_{dc})+b_1(2CL_1-1.5T_sCL_1KV_{dc})+1.5T_sCL_1b_2$ | | |
| $n_3=2b_0+b_1(1.5T_s+2CL_1KV_{dc})+b_2(2CL_1-1.5T_sCL_1KV_{dc})+1.5T_sCL_1b_3$ | | |
| $n_4=2b_1+b_2(1.5T_s+2CL_1KV_{dc})+b_3(2CL_1-1.5T_sCL_1KV_{dc})+1.5T_sCL_1b_4$ | | |
| $n_5=2b_2+b_3(1.5T_s+2CL_1KV_{dc})+b_4(2CL_1-1.5T_sCL_1KV_{dc})$ | | |
| $n_6=2b_3+b_4(1.5T_s+2CL_1KV_{dc})$ | | $n_7=2b_4$ |
| $a_0=-1.5T_sk_p$ | $a_1=2k_p-1.5T_s(k_p\omega_0+k_i)$ | |

This article has been accepted for publication in a future issue of this journal, but has not been fully edited. Content may change prior to final publication. Citation information: DOI 10.1109/TPEL.2018.2867610, IEEE Transactions on Power Electronics

| | | |
|---|---|---|
| $a_2 = 2k_p\omega_0 + 2k_i - 1.5T_s k_p\omega_0^2 + 3T_s\omega_0 k_i$ | | |
| $a_3 = 2k_p\omega_0^2 + 4k_i\omega_0 - 1.5T_s k_p\omega_0^3 + 1.5T_s k_i\omega_0^2$ | $a_4 = 2k_p\omega_0^3 - 2k_i\omega_0^2$ | |
| $b_0 = 1.5T_s$ | $b_1 = 2 + 1.5T_s\omega_0$ | $b_2 = 2\omega_0 + 1.5T_s\omega_0^2$ |
| $b_3 = 2\omega_0^2 + 1.5T_s\omega_0^3$ | $b_4 = 2\omega_0^3$ | $e_0 = 1.5T_s CL_1L_2$ |
| $e_1 = 2CL_1L_2 - 1.5T_s CL_2KV_{dc}$ | $e_2 = 2CL_2KV_{dc} + 1.5T_s(L_1 + L_2)$ | $e_3 = 2(L_1 + L_2)$ |

## REFERENCE


[1] F. Blaabjerg, R. Teodorescu, M. Liserre and A. V. Timbus, "Overview of control and grid synchronization for distributed power generation systems," *IEEE Trans. Ind. Electron*., vol. 53, no. 5, pp. 1398-1409, Oct. 2006.

[2] L. Harnefors, X. Wang, A. G. Yepes, and F. Blaabjerg, "Passivity-based stability assessment of grid-connected VSCs – an overview," *IEEE J. Emerg. Sel. Topics Power Electron*., vol. 4, no. 1, pp. 116-125, Mar. 2016.

[3] M.Malinowski, K. Gopakumar, J. Rodriguez, andM. A. Perez, "A survey on cascaded multilevel inverters," *IEEE Trans. Ind. Electron*., vol. 57, no. 7, pp. 2197–2206, Jul. 2010.

[4] A. Ajami, M. R. J. Oskuee, M. T. Khosroshahi, and A. Mokhberdoran," Cascade-multi-cell multilevel converter with reduced number of switches," *IET Power Electron*., vol. 7, no. 3, pp. 552–558, Mar. 2014.

[5] C. D. Townsend, T. J. Summers and R. E. Betz, "Multigoal Heuristic Model Predictive Control Technique Applied to a Cascaded H-bridge StatCom," *IEEE Trans. Power Electron.*, vol. 27, no. 3, pp. 1191-1200, March 2012.

[6] M. F. M. Elias, N. A. Rahim, H. W. Ping, and M. N. Uddin, "Asymmetrical Cascaded Multilevel Inverter Based on Transistor-Clamped H-Bridge Power Cell," *IEEE Trans. Ind. Appl.*, vol. 50, no. 6,pp. 4281–4288, Nov. 2014.

[7] A. Mortezaei, M. G. Simões, A. S. Bubshait, T. D. C. Busarello, F. P. Marafão and A. Al-Durra, "Multifunctional Control Strategy for Asymmetrical Cascaded H-Bridge Inverter in Microgrid Applications," *IEEE Trans. on Ind Application.*, vol. 53, no. 2, pp. 1538-1551, March-April 2017.

[8] H. Belkamel, S. Mekhilef, A. Masaoud, and M. A. Naeim, "Novel three-phase asymmetrical cascaded multilevel voltage source inverter," *IET Power Electron*., vol. 6, no. 8, pp. 1696–1706, Sep. 2013.

[9] F. Khoucha, M. S. Lagoun, A. Kheloui and M. E. H. Benbouzid, "A Comparison of Symmetrical and Asymmetrical Three-Phase H-Bridge Multilevel Inverter for DTC Induction Motor Drives," *IEEE Trans. Energy Convers.*, vol. 26, no. 1, pp. 64-72, March 2011.

[10] R. T. H. Li, C. N. M. Ho and E. X. Chen, "Active virtual ground— single-phase transformerless grid-connected voltage source inverter topology," *IEEE Trans. Power Electron.*, vol. 33, no. 2, pp. 1335-1346, Feb. 2018.

[11] Z. Aleem and M. Hanif, "Operational Analysis of Improved Γ-Z-Source Inverter With Clamping Diode and Its Comparative Evaluation," *IEEE Trans. Ind. Electron*., vol. 64, no. 12, pp. 9191-9200, Dec. 2017.

[12] L. He and C. Cheng, "A Flying-Capacitor-Clamped Five-Level Inverter Based on Bridge Modular Switched-Capacitor Topology," *IEEE Trans. Ind. Electron.*, vol. 63, no. 12, pp. 7814-7822, Dec. 2016.

[13] N. Hatano and T. Ise, "Control Scheme of Cascaded H-Bridge STATCOM Using Zero-Sequence Voltage and Negative-Sequence Current," *IEEE Trans. Power Deliv.*, vol. 25, no. 2, pp. 543-550, April 2010.

[14] M. N. A. Abdul Kadir and Z. F. Hussien, "Asymmetrical Multilevel Inverter: Maximum Resolution for H-Bridge Topology," 2005 *International Conference on Power Electronics and Drives Systems*, Kuala Lumpur, 2005, pp. 1068-1071.

[15] J. Lamb and B. Mirafzal, "An Adaptive SPWM Technique for Cascaded Multilevel Converters With Time-Variant DC Sources," *IEEE Trans. Ind. Appl.*, vol. 52, no. 5, pp. 4146-4155, Sept.-Oct. 2016.

[16] D. Yang, X. Ruan and H. Wu, "A Real-Time Computation Method With Dual Sampling Mode to Improve the Current Control Performance of the LCL-Type Grid-Connected Inverter," *IEEE Trans. Ind. Electron.*, vol. 62, no. 7, pp. 4563-4572, July 2015.

[17] M. Lu, A. Al-Durra, S. M. Muyeen, S. Leng, P. C. Loh and F. Blaabjerg, "Benchmarking of Stability and Robustness against Grid Impedance Variation for LCL-Filtered Grid-Interfacing Inverters," *IEEE Trans. Power Electron.*, vol. PP, no. 99, pp. 1-1,2017

[18] J. Wang, J. D. Yan and L. Jiang, "Pseudo-Derivative-Feedback Current Control for Three-Phase Grid-Connected Inverters With LCL Filters," *IEEE Trans. Power Electron.*, vol. 31, no. 5, pp. 3898-3912, May 2016.

[19] Y. Jia, J. Zhao and X. Fu, "Direct Grid Current Control of LCL-Filtered Grid-Connected Inverter Mitigating Grid Voltage Disturbance," *IEEE Trans. Power Electron.*, vol. 29, no. 3, pp. 1532-1541, March 2014.

[20] Y. Liu, W. Wu, Y. He, Z. Lin, F. Blaabjerg and H. S. H. Chung, "An Efficient and Robust Hybrid Damper for LCL- or LLCL-Based Grid-Tied Inverter With Strong Grid-Side Harmonic Voltage Effect Rejection," *IEEE Trans. Ind. Electron.*, vol. 63, no. 2, pp. 926-936, Feb. 2016.

[21] D. Dong, B. Wen, D. Boroyevich, P. Mattavelli and Y. Xue, "Analysis of Phase-Locked Loop Low-Frequency Stability in Three-Phase Grid-Connected Power Converters Considering Impedance Interactions," *IEEE Trans. Ind. Electron.*, vol. 62, no. 1, pp. 310-321, Jan. 2015.

[22] P. Rodriguez, A. Luna, I. Candela, R. Mujal, R. Teodorescu and F. Blaabjerg, "Multiresonant Frequency-Locked Loop for Grid Synchronization of Power Converters Under Distorted Grid Conditions," *IEEE Trans. Ind. Electron.*, vol. 58, no. 1, pp. 127-138, Jan. 2011.

[23] A. Safayet, I. Husain, A. Elrayyah and Y. Sozer, "Grid harmonics and voltage unbalance effect elimination for three-phase PLL grid synchronization algorithm," 2013 *IEEE Energy Conversion Congress and Exposition*, Denver, CO, 2013, pp. 3299-3304.

[24] S. Golestan, J. M. Guerrero, A. Abusorrah, M. M. Al-Hindawi and Y. Al-Turki, "An Adaptive Quadrature Signal Generation-Based Single-Phase Phase-Locked Loop for Grid-Connected Applications," *IEEE Trans. Ind. Electron.*, vol. 64, no. 4, pp. 2848-2854, April 2017.

[25] M. Céspedes and J. Sun, "Impedance shaping of three-phase grid-parallel voltage-source converters," 2012 *Twenty-Seventh Annual IEEE Applied Power Electronics Conference and Exposition* (APEC), Orlando, FL, 2012, pp. 754-760.

[26] M. Cespedes and J. Sun, "Impedance modeling and analysis of grid connected voltage-source converters," *IEEE Trans. Power Electron.*, vol. 29, no. 3, pp. 1254-1261, Mar. 2014

[27] S. Zhou et al., "An Improved Design of Current Controller for LCL-Type Grid-Connected Converter to Reduce Negative Effect of PLL in Weak Grid," *IEEE J. Emerg. Sel. Topics Power Electron.*, vol. PP, no. 99, pp. 1-1, 2017

[28] X. Wang, L. Harnefors and F. Blaabjerg, "Unified impedance model of grid-connected voltage-source converters," *IEEE Trans. Power Electron.*, vol. 33, no. 2, pp. 1775-1787, Feb. 2018.

[29] S. Lissandron, L. Dalla Santa, P. Mattavelli and B. Wen, "Experimental Validation for Impedance-Based Small-Signal Stability Analysis of Single-Phase Interconnected Power Systems With Grid-Feeding Inverters," *IEEE Journal of Emerging and Selected Topics in Power Electronics*, vol. 4, no. 1, pp. 103-115, March 2016.

[30] M. K. Bakhshizadeh, X. Wang, F. Blaabjerg, J. Hjerrild, L. Kocewiak, C. L. Bak, and B. Hesselbaek, "Couplings in phase domain impedance modeling of grid-connected converters," *IEEE Trans. Power Electron.*, vol. 31, no. 10, pp. 6792-6796, Oct. 2016.

[31] V. Salis, A. Costabeber, P. Zanchetta and S. Cox, "Stability analysis of single-phase grid-feeding inverters with PLL using Harmonic Linearisation and Linear Time Periodic (LTP) theory," 2016 IEEE 17th Workshop on Control and Modeling for Power Electronics (COMPEL), Trondheim, 2016, pp. 1-7.

[32] R. Fantino, C. Busada, and J. Solsona, "Optimum PR control applied to LCL filters with low resonance frequency," IEEE Trans. Power Electron., vol.33, no.1, pp. 793-801, 2018

[33] X. A. Fu, and S. H. Li, "Control of single-phase grid-connected converters with LCL filters using recurrent neural network and conventional control methods," IEEE Trans. Power Electron., vol. 31, no. 7, pp. 5354-5364, Jul. 2016.

[34] Y. Han, X. Fang, P. Yang, C. Wang, L. Xu and J. M. Guerrero, "Stability Analysis of Digital Controlled Single-Phase Inverter with Synchronous Reference Frame Voltage Control," *IEEE Trans. Power Electron.*, vol. 33, no. 7, pp. 6333-6350, 2018

[35] M. Monfared, S. Golestan, and J. M. Guerrero, "Analysis, design, and experimental verification of a synchronous reference frame voltage control for single-phase inverters," *IEEE Trans. Ind. Electron.*, vol. 61, no. 1, pp. 258-269, Jan. 2014.

[36] S. Kouro, R. Bernal, H. Miranda, J. Rodriguez, and J. Pontt, "Direct torque control with reduced switching losses for asymmetric multilevel inverter fed induction motor drives," 2006 *IEEE Industry Applications Conference Forty-First IAS Annual Meeting*, Tampa, FL, 2006, pp. 2441-2446.

[37] X. Zhang, J. W. Spencer and J. M. Guerrero, "Small-Signal Modeling of Digitally Controlled Grid-Connected Inverters With LCL Filters," IEEE Transactions on Industrial Electronics, vol. 60, no. 9, pp. 3752-3765, Sept. 2013.

[38] J. L. Agorreta, M. Borrega, J. López and L. Marroyo, "Modeling and Control of N -Paralleled Grid-Connected Inverters With LCL Filter Coupled Due to Grid Impedance in PV Plants," IEEE Transactions on Power Electronics, vol. 26, no. 3, pp. 770-785, March 2011.

[39] R. W. Erickson and D. Maksimovic, Fundamentals of Power Electronics. Springer Science & Business Media, 2007.

[40] J. L. Agorreta, M. Borrega, J. López and L. Marroyo, "Modeling and Control of N -Paralleled Grid-Connected Inverters With LCL Filter Coupled Due to Grid Impedance in PV Plants," *IEEE Trans. Power Electron.*, vol. 26, no. 3, pp. 770-785, March 2011.

[41] X. Chen, Y. Zhang, S. Wang, J. Chen and C. Gong, "Impedance-phased dynamic control method for grid-connected inverters in a weak grid," *IEEE Trans. Power Electron.*, vol. 32, no. 1, pp. 274-283, Jan. 2017.
[42] C. Zhang, X. Wang and F. Blaabjerg, "Analysis of phase-locked loop influence on the stability of single-phase grid-connected inverter," 2015 IEEE 6th International Symposium on Power Electronics for Distributed Generation Systems (PEDG), Aachen, 2015, pp. 1-8.
[43] J. Sun, "Impedance-based stability criterion for grid-connected inverters," *IEEE Trans. Power Electron.*, vol. 26, no. 11, pp. 3075-3078, Nov. 2011.
[44] Y. F. Wang and Y. W. Li, "Grid synchronization PLL based on cascaded delayed signal cancellation," *IEEE Trans. Power Electron.*, vol. 26, no. 7, pp. 1987-1997, July 2011.

**Yang Han** (S'08-M'10-SM'17) received the Ph.D. degree in Electrical Engineering from Shanghai Jiaotong University (SJTU), Shanghai, China, in 2010. He joined the Department of Power Electronics, School of Mechatronics Engineering, University of Electronic Science and Technology of China (UESTC) in 2010, and has been an Associate Professor since 2013. From March 2014 to March 2015, he was a visiting scholar at the Department of Energy Technology, Aalborg University, Aalborg, Denmark. Currently, he is with the Department of Electrical Engineering, School of Mechanical and Electrical Engineering, UESTC. His research interests include the AC/DC microgrids, grid-connected converters for renewable energy systems, power quality, active power filters, multilevel converters and static synchronous compensators (STATCOMs).

He has authored more than 20 ISI-indexed international journal papers and one book chapter in the area of power elctronics, power quality conditoners and smart grid. He has served as Session Chair in "Microgrid Optimization and Scheduling" Session in the 2nd International Conference on Power and Renewable Energy, Chengdu, China, in 2017, in "Power Quality Mitigation and Application" Session in the 5th National Conference on Power Quality in Xi'an in 2017, and in "AC/DC, DC/AC Power Converter" Session in the 2016 IPEMC ECCE-Asia in Hefei, China. He was awarded the "Academic Talent Award" by UESTC in 2017, and "Baekhyun Award" by the Korean Institute of Power Electronics (KIPE) in 2016. He received Best Paper Awards from the 6th Asia International Symposium on Mechatronics in 2017, the 5th National Conference on Power Quality in 2017, the Annual Conference of HVDC and Power Electronics Committee of Chinese Society of Electrical Engineers (CSEE) in 2013, and the 4th International Conference on Power Quality in 2008, China. He holds 18 issued and ten pending patents. He is an active reviewer of the IEEE Transactions on Power Electronics, IEEE Transactions on Industrial Electronics, IEEE Transactions on Smart Grid, and IEEE Industrial Electronics Magazine.

**Hao Chen** received the B.S. degree in Automation from Southwest University of Science and Technology, Mianyang, China, in 2016. He is currently working towards the M.S. degree in Power Electronics and Electric Drives at the University of Electronic Science and Technology of China (UESTC), Chengdu, China. His current research interests include system modeling and stability analysis of power electronic converters, power quality management, and control methods of distributed generation systems.

**Zipeng Li** received the B. S. degree in electrical engineering and automation from Sichuan Normal University, Chengdu, China, in 2014, and the M. S. degree in power electronics and electric drive from UESTC, Chengdu, China, in 2017, and joined the State Grid Guanghan City Electric Power Supply Branch, Guanghan, China, in 2017. His current research interests include the modelling and control of power electronics, multilevel converters, digital signal processing (DSP), and digital simulation of the grid-connected PV power plants.

**Ping Yang** received the B.S. in Mechanical Engineering from Shanghai Jiaotong University (SJTU), Shanghai, China, in 1984, and the M. S. in Mechanical Engineering from Sichuan University in 1987, respectively. He is currently a full professor with the School of Mechatronics Engineering, University of Electronic Science and Technology of China (UESTC), Chengdu, China. He was visiting the Victory University, Australia from July 2004 to August 2004, and a visiting scholar with the S. M. Wu Manufacturing Research Center, University of Michigan, Ann Arbor, USA, from August 2009 to February 2010, and was visiting the University of California, Irvine, USA, from October 2012 to November 2012.

His research includes mechatronics engineering, electrical engineering and automation, computer-aided control and instrumentation, smart mechatronics, and detection and automation of mechanical equipment. He has authored more than 60 papers in various journals and international conferences, and several books on mechatronics and instrumentation. He received several provincial awards for his contribution in teaching and academic research. He is currently the Dean of the School of Mechanical and Electrical Engineering, UESTC.

**Lin Xu** received the Ph.D. degree in Electrical Engineering from Shanghai JiaoTong University (SJTU), Shanghai, China, in 2011. Currently, she is a Senior Engineering at Sichuan Electric Power Research Institute, State Grid Sichuan Electric Power Company, Chengdu, China. She has co-authored more than 20 journal and conference papers in the area of power electronics and power systems.

Her research interests include power quality, power system analysis and real-time digital simulator (RTDS), flexible Ac transmission systems (FACTS), such as STATCOMs and power quality conditioners (DVRs, APFs). She is an active reviewer for IEEE Transactions on Industrial Electronics, IEEE Transactions on Power Electronics, Electric Power Components and Systems, etc.

**Josep M. Guerrero** (S'01-M'04-SM'08-FM'15) received the B.S. degree in telecommunications engineering, the M.S. degree in electronics engineering, and the Ph.D. degree in power electronics from the Technical University of Catalonia, Barcelona, in 1997, 2000 and 2003, respectively. Since 2011, he has been a Full Professor with the Department of Energy Technology, Aalborg University, Denmark, where he is responsible for the Microgrid Research Program. From 2012 he is a guest Professor at the Chinese Academy of Science and the Nanjing University of Aeronautics and Astronautics; from 2014 he is chair Professor in Shandong University; from 2015 he is a distinguished guest Professor in Hunan University; and from 2016 he is a visiting professor fellow at Aston University, UK.

His research interests is oriented to different microgrid aspects, including power electronics, distributed energy-storage systems, hierarchical and cooperative control, energy management systems, smart metering and the internet of things for AC/DC microgrid clusters and islanded minigrids; recently specially focused on maritime microgrids for electrical ships, vessels, ferries and seaports. Prof. Guerrero is an Associate Editor for the IEEE TRANSACTIONS ON POWER ELECTRONICS, the IEEE TRANSACTIONS ON INDUSTRIAL ELECTRONICS, and the IEEE Industrial Electronics Magazine, and an Editor for the IEEE TRANSACTIONS on SMART GRID and IEEE TRANSACTIONS on ENERGY CONVERSION. He has been Guest Editor of the IEEE TRANSACTIONS ON POWER ELECTRONICS Special Issues: Power Electronics for Wind Energy Conversion and Power Electronics for Microgrids; the IEEE TRANSACTIONS ON INDUSTRIAL ELECTRONICS Special Sections: Uninterruptible Power Supplies systems, Renewable Energy Systems, Distributed Generation and Microgrids, and Industrial Applications and Implementation Issues of the Kalman Filter; the IEEE TRANSACTIONS on SMART GRID Special Issues: Smart DC Distribution Systems and Power Quality in Smart Grids; the IEEE TRANSACTIONS on ENERGY CONVERSION Special Issue on Energy Conversion in Next-generation Electric Ships. He was the chair of the Renewable Energy Systems Technical Committee of the IEEE Industrial Electronics Society. He received the best paper award of the IEEE Transactions on Energy Conversion for the period 2014-2015. In 2014 and 2015 he was awarded by Thomson Reuters as Highly Cited Researcher, and in 2015 he was elevated as IEEE Fellow for his contributions on "distributed power systems and microgrids."